12-2022

Nucleation and Growth of Molybdenum Disulfide Grown by Thermal Atomic Layer Deposition on Metal Oxides

Jake Soares
Boise State University

Steven Letourneau
Boise State University

Matthew Lawson
Boise State University

Yu Lu
Boise State University

Yaqiao Wu
Boise State University

See next page for additional authors

Publication Information

Jake Soares; Steven Letourneau; Matthew Lawson; Anil U. Mane; Yu Lu; Yaqiao Wu; . . . and Elton Graugnard. (2022). "Nucleation and Growth of Molybdenum Disulfide Grown by Thermal Atomic Layer Deposition on Metal Oxides". *Journal of Vacuum Science & Technology A, 40*(6), 062202. https://doi.org/10.1116/6.0002024

Nucleation and growth of molybdenum disulfide grown by thermal atomic layer deposition on metal oxides

Running title: MoS_2 ALD Nucleation

Running Authors: Soares *et al*.

Jake Soares[1], Steven Letourneau[1,2], Matthew Lawson[1], Anil U. Mane[2], Yu Lu[1,3], Y.Q. Wu[1,3], Steven M. Hues[1], Lan Li[1,3], Jeffrey W. Elam[2], and Elton Graugnard[1,3,a)]

[1]Micron School of Materials Science and Engineering, Boise State University, 1910 University Dr., Boise, ID 83725, USA

[2]Applied Materials Division, Argonne National Laboratory, 9700 S Cass Ave, Lemont, IL 60439, USA

[3]Center for Advanced Energy Studies, Idaho Falls, ID 83401, US

[a)]Electronic mail: Eltongraugnard@boisestate.edu

To enable greater control over the thermal atomic layer deposition (ALD) of molybdenum disulfide (MoS_2), here we report studies of the reactions of molybdenum hexafluoride (MoF_6) and hydrogen sulfide (H_2S) with metal oxide substrates from nucleation to few-layer films. *In situ* quartz crystal microbalance (QCM) experiments performed at 150, 200, and 250 ºC revealed temperature-dependent nucleation behavior of the MoF_6 precursor, which is attributed to variations in surface hydroxyl concentration with temperature. *In situ* Fourier transform infrared spectroscopy (FTIR), coupled with *ex situ* X-ray photoelectron spectroscopy (XPS) indicated the presence of molybdenum oxide and molybdenum oxyfluoride species during nucleation. Density functional theory calculations additionally support the formation of these species, as well as predicted metal oxide to fluoride conversion. Residual gas analysis revealed reaction byproducts, and the combined experimental and computational results provided insights for proposed

nucleation surface reactions. With additional ALD cycles, Fourier transform infrared spectroscopy indicated steady film growth after ~13 cycles at 200 ºC. XPS revealed that higher deposition temperatures resulted in a higher fraction of MoS_2 within the films. Deposition temperature was found to play an important role in film morphology with amorphous films obtained at 200 °C and below, while layered films with vertical platelets were observed at 250 °C. These results provide an improved understanding of MoS_2 nucleation, which can guide surface preparation for the deposition of few-layer films and advance MoS_2 toward integration into device manufacturing.

I. INTRODUCTION

Layered two-dimensional (2D) molybdenum disulfide (MoS_2), along with many other transition metal chalcogenides, has been the focus of intense research in the past several years[1, 2, 3]. As a 2D semiconductor with a 2.4 eV direct one-electron quasiparticle electronic band gap in monolayer form[4], MoS_2 is a promising material for applications in electronics[5], optoelectronics[6, 7], photovoltaics[8-10], and energy conversion[11-13]. As with any material, to be commercially viable, many of these applications require industry-compatible high-volume manufacturing techniques. For MoS_2, two promising, industrially scalable techniques are chemical vapor deposition (CVD) and atomic layer deposition (ALD). CVD can produce high quality MoS_2 but doing so requires temperatures that are often too high for device integration[14-16]. As a variant of CVD, ALD achieves lower deposition temperatures by employing chemical precursors with higher reactivities. However, ALD relies on sequential surface reactions, and these reactions can vary for deposition on different substrates, resulting in differences in the nucleation and growth behavior of the deposited films. Since a monolayer of MoS_2 is a three atom thick film of ~0.6-0.7 nm[17], only a small number of ALD cycles should be needed to grow few-layer films. However, many ALD chemistries have an incubation period where the growth per cycle varies with cycle number and an interphase can form during the transition from nucleation to growth[18]. Understanding this transition is crucial, as this early growth regime can constitute the entirety of a few-layer film. Some work has been done to investigate the nucleation and growth of MoS_2 films as grown by a variety of techniques. These include nucleation studies from CVD grown MoS_2 on SiO_2[19, 20], graphene[21] and quartz[22]. As well as investigations of the kinetic growth by a vapor-liquid-adatom-solid process[23]. Understanding the early stages of growth and nucleation is increasingly important as it dictates the quality of crystalline MoS_2 film that is deposited, but

also can provide insight into possible interface formation between the MoS_2 film and substrate material. These interfaces can profoundly impact device performance.

Here, we report *in situ* and *ex situ* characterization studies of the nucleation and growth of few-layer MoS_2 films deposited via thermal atomic layer deposition using MoF_6 and H_2S precursors on ALD-grown aluminum oxide (alumina), hafnium oxide (hafnia), and magnesium oxide (magnesia). These metal oxides were selected based on their relevance to MoS_2 electronic devices, range of surface chemical properties, and well-established ALD processes that facilitate detailed *in situ* studies. The early growth regimes on each of these oxides were investigated utilizing *in situ* quartz crystal microbalance[24, 25] (QCM) measurements and *in situ* Fourier transform infrared (FTIR) spectroscopy[26]. These measurements probe the interfacial chemical reactions during the ALD half cycles to help understand the complex surface interactions between the metal oxide and the precursors. *Ex situ* characterization using X-ray photoelectron spectroscopy (XPS), Raman spectroscopy, and transmission electron microscopy (TEM) of both as-deposited and annealed MoS_2 films provided information about chemical bonding and confirmed layering of the material, either upon annealing or during growth at ~250 °C. Our results provide insights into the growth of MoS_2 on metal oxide surfaces and advance efforts toward manufacturing of few-layer MoS_2 films.

II. EXPERIMENT

A. Growth

ALD growth and *in situ* measurements were performed in custom viscous flow reactors at both Boise State University and Argonne National Laboratory[24]. The process pressures of the reactors were between 0.5-1.5 Torr by flowing 40-200 sccm of ultra-high purity nitrogen (99.999% Norco) or argon (99.999% Airgas) as carrier gasses. Growth and thickness control

were achieved by repeating single ALD cycles for binary (A + B) chemistries. Each ALD cycle consists of four steps: (1) dose of reactant A, (2) purge of by-products and excess reactant, (3) dose of reactant B, and (4) purge of remaining by-products and excess reactant. For given precursor partial pressures, exposure times were controlled by computer operated pneumatic valves and are expressed in seconds as t_1-t_2-t_3-t_4 for the four steps of an ALD cycle.

The substrates for molybdenum disulfide (MoS_2) ALD consisted of Si(100) coupons with native oxide that were coated with ALD alumina, hafnia, and magnesia films. In some cases, the ALD metal oxide films were deposited immediately before the MoS_2 ALD without exposure to ambient (*in situ* substrates). In other cases, the substrates were exposed to ambient conditions before the MoS_2 ALD (*ex situ* substrates). The ALD alumina, hafnia, and magnesia were deposited using trimethylaluminum (TMA, Sigma Aldrich or Strem Chemicals, 97+%), tetrakis(dimethylamino)hafnium (TDMAH, Strem Chemicals, 98+%), and bis(cyclopentadienyl)magnesium(II) ($Mg(cp)_2$, Strem Chemicals, 99.9+%) as the metal precursor, respectively, and nanopure deionized H_2O as the oxygen source. The TMA and H_2O were maintained at room temperature and dosed through metering valves to control their partial pressures in the ALD reactor. The TDMAH and $Mg(cp)_2$ were held in stainless-steel bubblers heated to 150 ºC and 65 ºC, respectively, and inert gas was flown through the bubblers during dosing. Prior to the MoS_2 ALD, the *ex situ* substrates were cleaned in fuming sulfuric acid for 10 min, rinsed with nanopure water, dried with nitrogen and stored in a vacuum desiccator. *Ex situ* magnesia samples were further annealed at 700 °C for 30 minutes to remove excess water[27, 28]. The *ex situ* hafnia and magnesia substrates were provided by Micron Technology.

The MoS_2 ALD was performed using alternating exposures to molybdenum hexafluoride (MoF_6, Sigma Aldrich or Synquest Laboratories, 98%) and hydrogen sulfide (H_2S, Matheson

Trigas or Sigma Aldrich, 99.5%). These compressed gas precursors were stored in lecture bottles with two-stage regulators and delivered through 200 μm orifices and metering valves to reduce their partial pressures in the ALD reactor. Additionally, the H_2S manifold had a pressure regulator in line, limiting the pressure to 1 atm. Unless stated otherwise, following deposition, films were annealed at 600 ºC in H_2S at ~2 Torr for 30 min. to form a layered structure[29].

B. Characterization

The *in situ* quartz crystal microbalance (QCM) measurements were performed using a modified Maxtek Model BSH-150 sensor head or an Inficon ALD Sensor. RC cut crystals with an alloy coating (Phillip Technologies and Inficon) were used in the QCM sensors. To prevent deposition on the backside of the crystal, the backside was purged with carrier gas that was tuned to ~10% of the system base pressure. Prior to QCM measurements, the reactor temperatures were allowed to stabilize for several hours to reduce the temperature-dependent frequency drift of the crystal. To improve consistency between experiments, 50-100 cycles of metal oxide ALD were performed to passivate the reactor walls and QCM sensor surface.

In situ Fourier transform infrared (FTIR) spectroscopy measurements were conducted in a separate ALD system described in previous reports[30, 31]. The sample substrate consisted of ZrO_2 nanopowder pressed into a stainless-steel grid. The ZrO_2 nanopowder was coated with ALD alumina prior to the *in situ* FTIR measurements of the metal oxide and MoS_2 to provide a consistent starting surface. During the ALD precursor exposures, gate valves in front of the IR-transparent KBr windows were closed to prevent deposition on the windows[32]. The FTIR transmission spectra were collected using a Nicolet 6700 FTIR spectrometer (Thermo Scientific) interfaced to a control computer. Because of the high surface area of the ZrO_2 nanopowder,

longer exposure and purge times were used compared to the *in situ* QCM and measurements and substrate coating experiments.

In situ residual gas analysis (RGA) measurements were conducted using an Extorr XT200 operated in trend mode to monitor H_2O (m/e = 18), HF (m/e = 20), and F_2 (m/e = 38) gas species. To confidently determine ALD byproducts a dosing scheme during the ALD process was AAA – purge – BBB – purge to distinguish reaction byproducts from background gases. To increase the signal of byproducts formed the chamber was filled with additional substrate material consisting of SiO_2 coupons and a woven alumina cloth (Zircar Inc.) to increase functional surface area. Increased pulse times of precursors were additionally used to ensure saturation across substrates. All substrate materials were coated with ~10 nm of alumina prior to MoS_2 precursor exposure.

X-ray photoelectron spectroscopy (XPS) measurements were performed using either a Thermo Scientific K-Alpha or Physical Electronics (PHI) 5600 ESCA system operating in standard lens modes. Both systems used a monochromated Al K-alpha sources. The XPS data were analyzed using Thermo Scientific Avantage software (Thermo Scientific system) or MultiPak 9.6 (PHI system). All spectra were referenced to the 1s peak (284.8 eV) of adventitious carbon. See supplementary material at [URL will be inserted by AIP Publishing] for additional details related to XPS analysis and instrument set up.

Raman spectroscopy was performed using either a Renishaw inVia or a Horiba LabRAM system in reflection mode with 514 or 532 nm excitation sources, respectively. Spectra were acquired over the 340-440 cm^{-1} range to capture the primary E^1_{2g} and A_{1g} modes of MoS_2.

Cross-sectional TEM samples were prepared on planar coupons for MoS_2 studies. To protect the delicate MoS_2 layer and to ensure the chemical composition was not altered during

FIB process, samples were first coated with 50nm gold using a Hummer 6.2 sputtering system. After coating, the samples were loaded to a FEI (now ThermoFisher) Quanta 3D dual-beam Focused Ion Beam (FIB) for TEM lamella preparation by using the lift-out technique. Inside the FIB, a 2 μm thick Pt layer was deposited to the sample surface at the beginning. This Pt layer is intended to protect the sample from any potential FIB damage during the FIB milling. For the last step inside FIB, both sides of the lamella were milled with 2 kV Ga^+ to minimize the damage from FIB. In this way, the delicate layer remained intact to the largest extent during the TEM lamella process. TEM characterization was carried out by using a FEI (now ThermoFisher) Tecnai G2 F30 STEM. Carbon nanotube images were acquired with a LaB_6 JEOL JEM-2100 TEM microscope at 200 keV. Hydroxylated multiwall carbon nanotubes (CNTs) (Nanostructured & Amorphous Materials, Inc.) were dispersed in ~2 mL of ethanol, sonicated for 10 minutes, and then drop cast onto 400 mesh stainless steel TEM grids (Ted Pella, Inc). Roughly 6-8 nm of ALD alumina and hafnia were deposited onto separate CNT samples prior to MoS_2 ALD.

Spectroscopic ellipsometry (SE) thickness measurements were taken on a J.A. Woollam M-2000 in the spectral range of 250-1680 nm. On each sample, three-point scans were taken at angles of incidence of 50°, 60°, and 70°, reported values are from calculated averages. SE data were fit using CompleteEASE 5.10 (J.A. Woollam). The data were fit with models made up of multi-layer film stacks consisting of Si substrate, native oxide interfacial SiO_2 layer, metal oxide layer and finally a MoS_2 film. A Tauc-Lorentz oscillator model was used for the MoS_2 film.

Atomic force microscopy (AFM) measurements were acquired with a Dimension FastScan (Bruker) operating in PeakForce tapping mode. ScanAsyst-air probes with a tip radius of 8 nm were used for imaging. Image processing was carried out in NanoScope Analysis 1.9.

III. MODELING

First-principles density functional theory (DFT)-based calculations were conducted using the Vienna Ab initio Simulation Package (VASP) using Perdew-Burke-Enzerhof (PBE) pseudopotentials with the generalized gradient approximation (GGA) exchange correlation functions. A cut-off energy of 400 eV was used, and residual forces were reduced to 0.01 eV/atom with an energy convergence test. The alumina surface was cleaved from a relaxed alumina unit cell, and a 2×2×1 supercell was created to increase surface area. A Monkhorst pack 5×5×1 k-point mesh was chosen for the alumina surfaces and a vacuum greater than 15 Å was introduced to mitigate spurious interactions. To reduce computational effort the bottom three layers were frozen using selective dynamics, while the top three layers had no restraints.

IV. RESULTS AND DISCUSSION

A. Nucleation

1. In situ QCM Measurements, Part 1

In situ QCM measurements were performed at 150, 200, and 250 ºC to evaluate hetero-nucleation and growth of MoS_2 on the metal oxide surfaces. The ALD metal oxides were deposited on the QCM surface until a steady mass gain per cycle (MGPC) was achieved that was close to the expected values of 41 ng/cm^2/cyc for alumina[25], 38 ng/cm^2/cyc for hafnia[33], and 44 ng/cm^2/cyc for magnesia[18, 34]. While the number of cycles of metal oxide and MoS_2 varied slightly, a typical experiment consisted of 50 cycles of metal oxide followed ~20-40 cycles of MoF_6 and H_2S with a pulse-purge-pulse-purge timing sequence of 1.5-15-1.5-15 (all times in seconds as described above). An extra 30 second purge was added between the metal oxide and

MoF_6/H_2S to allow for sufficient oxide precursor purge. To determine the extent of nucleation and establish the transition to steady growth, the mass change per cycle for ALD of MoS_2 was measured until a constant MGPC was observed.

In situ QCM measurements plotted in Fig. 1 show the first two ALD cycles of MoF_6 and H_2S on the surface of ALD alumina at 150, 200, and 250 ºC. For each temperature, a significant mass increase was observed during the initial MoF_6 pulse followed by a temperature-dependent mass decrease. This mass loss was approximately twice as large at 200 and 250 ºC compared to 150 ºC. These transient features may be temperature-induced frequency changes caused by exothermic chemistry on the QCM sensor. The initial net mass gain varied from 111 at 150 ºC to 67 ng/cm^2 at 250 ºC (Figure 1).

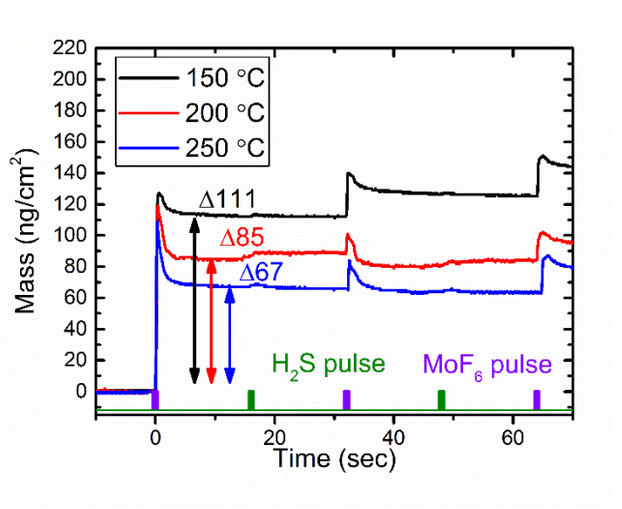

FIGURE 1. *In situ* QCM measurements of mass versus time for the first few cycles of MoS_2 ALD on alumina. Mass change for initial MoF_6 pulse can be seen for deposition temperatures of 150, 200, and 250 ºC. MoF_6 and H_2S pulses are indicated schematically. Temperature dependent mass gains can be observed with 150 ºC deposition temperature having the most initial mass gain after MoF_6.

Figure 1 shows a decrease in the mass gain for the first half cycle as the temperature increases. This could either reflect a decrease in the surface density of adsorbed MoF_x species, a decrease in the number of F atoms retained (x), or both. As will be discussed later, our studies indicate an overall lack of gaseous byproduct formation during the first half cycle. Thus, we attribute the decrease in mass gain to a lowering of surface reactivity as temperature increases. The surface density of adsorbed MoF_x species appears to be dependent on the surface hydroxyl concentration. Nelson *et al.* reported that the hydroxyl surface concentration decreases by approximately 62% between 150 and 250 ºC [35]. Calculating the relative change in net mass gain, (111 – 67)/111, we observe a decrease by 40%. The discrepancy could be caused by the increase in activity in MoF_6 at the higher temperature leading to non-self-limiting growth [36]. The large net mass gain at 150 ºC may also include contributions from physisorbed MoF_6 or reaction products. However, based on computational studies for nucleation of MoF_6 onto alumina, hafnia, and magnesia[37], the role of the hydroxyls is to aid in the dissociation of MoF_6 rather than to participate in a reaction directly. While the hydroxyls may be promoting dissociation rather than reacting with the MoF_6, the temperature dependence of the hydroxyl concentration would also result in reduced MoF_6 dissociation at higher temperatures.

In contrast to the alumina, both magnesia and hafnia exhibited more complicated mass differences with varied temperature. See supplementary material at [URL will be inserted by AIP Publishing] for *in situ* QCM measurements on both hafnia and magnesia surfaces. The first half cycles all exhibited large mass increases of ~100-200 ng/cm^2 compared to steady-state MGPC values of ~15-20 ng/cm^2. For both hafnia and magnesia, almost all initial mass gains were larger than those for alumina. While the temperature dependence for the first half cycle mass gains on alumina may be related to hydroxyl concentrations, the first half cycle mass gain temperature

dependence was more complicated on hafnia and magnesia. The hafnia surface (Figure S1(a)) shows an elevated mass gain for both the lowest and highest deposition temperatures 150 and 250 ºC, respectively. This behavior could reflect a similar OH-dependent dissociation at lower temperatures, while higher temperatures may reflect additional reaction pathways, possibly based on precursor residues from the hafnia ALD. The magnesia surface (Figure S1(b)) showed a similar large mass increase at 200 and 250 ºC, suggesting an energy barrier for the initial MoF_6 chemisorption. Based on FTIR spectra discussed next, the first half cycle reactions do appear to reflect more complex surface chemical reactions for MoF_6 deposition on hafnia and magnesia compared to alumina.

For each metal oxide and all temperatures, the second half cycle of the MoS_2 ALD produced almost no mass change. The negligible mass changes during the H_2S exposures indicates that the mass decrease from removal of HF and other species is roughly equivalent to the mass increase from sulfur addition.

2. In situ Fourier Transform Infrared Measurements, Part 1

FTIR spectroscopy can give insight into chemical bonding and identify the surface functional groups that participate in the ALD reactions. FTIR spectroscopy results from the alumina surface will be primarily reported on in this section. See supplementary material at [URL will be inserted by AIP Publishing] for FTIR data on magnesia and hafnia. Figure 2 shows *in situ* FTIR difference spectra recorded after each precursor exposure for the final cycle of alumina ALD and the first two cycles of MoS_2 ALD at temperatures of 150, 200, and 250 ºC. The FTIR spectra following the TMA and H_2O exposures for alumina ALD show characteristic "flip-flop" features from the addition and removal of surface hydroxyl (3200 to 3700 cm^{-1}) and methyl groups (3000 cm^{-1} and 1210 cm^{-1}) indicative of steady-state alumina growth[30]. Upon

MoF_6 exposure to the OH terminated alumina surface, a loss of a hydroxyl feature near 3700 cm^{-1} is observed as well as a decrease in the Al-O bulk modes from 1200 to 800 cm^{-1} (Figure 2(a-c)). Very few distinct features are observed within the measurement range for the first H_2S exposure. During the second cycle of MoF_6 and H_2S, a $MoOF_4$ mode can be seen forming near 1039 cm^{-1} [38, 39] during the MoF_6 pulse, in Figure 2(d-f). After the H_2S pulse, a loss of the $MoOF_4$ peak is observed, and a peak at 994 cm^{-1} emerges. This behavior is consistent with the formation of MoO_x species. Both MoO_3 and MoO_4^{2-} have overlapping peaks at 994 and 1007 cm^{-1} [40]. Additionally, modes have been identified in the 995-820 cm^{-1} range signifying the presence of MoO_3 [41]. The two primary bands that are seen may comprise multiple MoO_x species since $Mo(=O)_2$, Mo=O, and Mo-O all have modes in this range[40]. The net decrease in Al-O bulk modes combined with the appearance of MoO_x features suggest Mo-O-Al bonding, which is

expected at the interface between the MoS_2 and the alumina surface.

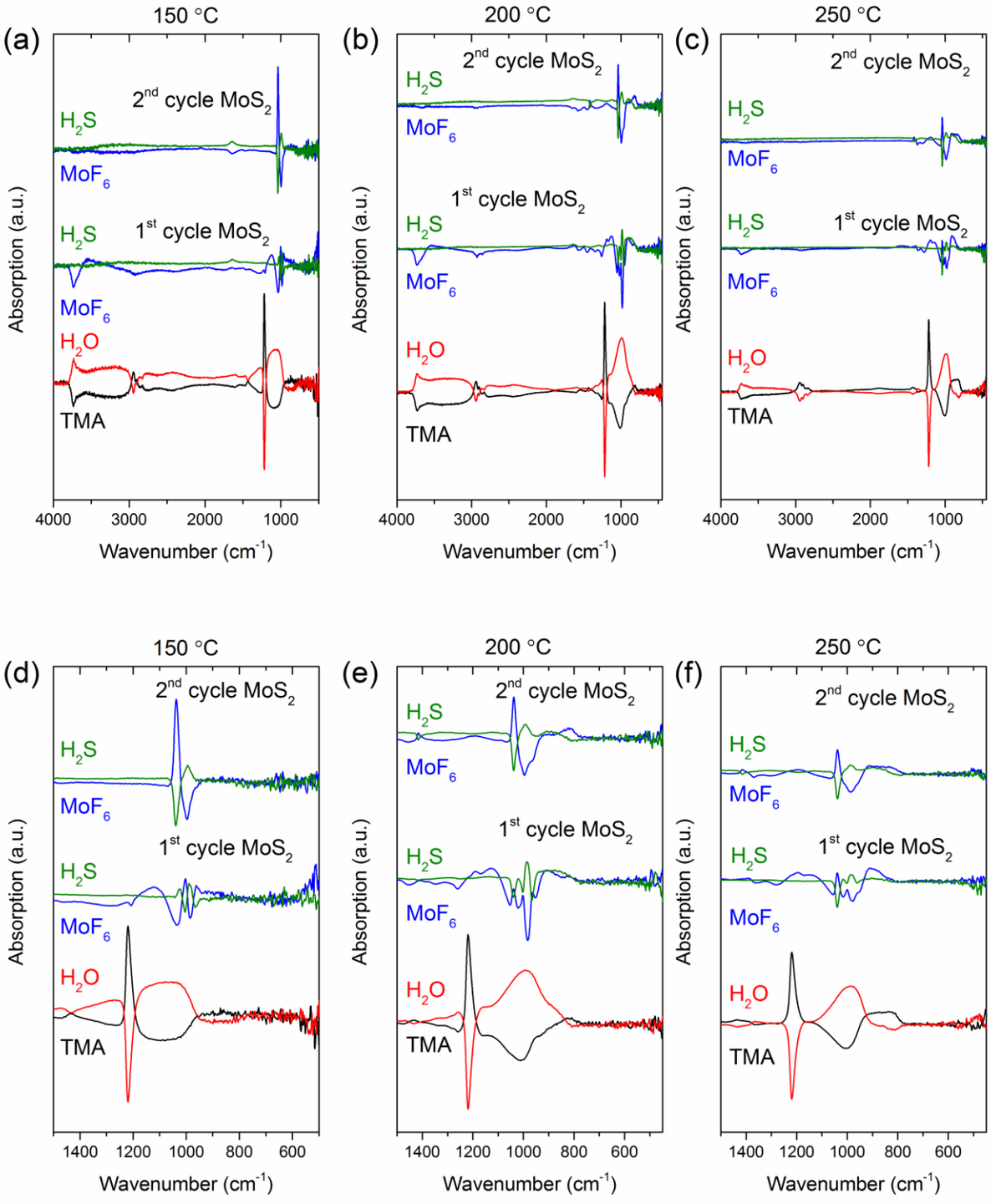

FIGURE 2. FTIR difference spectra for the last alumina cycle at 200 ºC and first two cycles of MoS_2 deposited at 150, 200, and 250 ºC. Plots (a-c) show the full spectra, where the OH stretches of the last water pulse (in red) can be seen above 3500 cm^{-1}. Plots (d-f) show expanded views of lower frequency portion of the spectra from 1500 to 550 cm^{-1} to highlight changes in the Al-O bulk modes and appearance of a $MoOF_4$ mode near 1039 cm^{-1}. Spectra are offset vertically for clarity.

The difference curves in Fig. 2 can obscure intensity shifts in the broad peaks. These shifts can be observed more clearly in the absolute absorption spectra shown in Fig. 3. After the initial MoF_6 pulse, a peak at 1002 cm^{-1} is observed. It would seem plausible to associate the 1002 peak to a MoO_x species, due to the proximity of a known 1007 cm^{-1} peak location[40]. However, we would expect this peak to persist in subsequent spectra since the Al-O-Mo interface should remain intact as the MoS_2 film grows. The absence of 1002 cm^{-1} peak in subsequent spectra suggests some type of Al-F bond since the only species present are Mo-O/F-Al. Indeed, a peak at this location was observed previously during *in situ* FTIR measurements of AlF_3 ALD although the peak was not assigned[42]. Further experiments are needed to assign this feature. The peak that appears after the second dose of MoF_6 at 1039 cm^{-1} has been assigned to the Mo=O stretch in $MoOF_4$ [38, 43]. Careful inspection of the difference spectra in Fig. 2 do reveal a feature at 1039 cm^{-1}, but it is overshadowed by the decrease in intensity from the Al-O bulk modes. After each H_2S dose, the $MoOF_4$ peak disappears in Fig. 3, which is seen as a negative intensity in Fig. 2. This observation suggests the conversion of the $MoOF_4$ species with liberation of F atoms through HF byproducts from the introduced H_2S. These spectral changes diminish with increasing MoS_2 ALD cycles indicating coalescence of the MoS_2 film. Due to absorption by the ZrO_2 nanopowder, our FTIR spectrometer was not sensitive below ~525 cm^{-1} where many of the Mo-S modes are located [44]. This limitation prevented confirmation of Mo-S bonding with *in situ* FTIR.

In situ FTIR measurements were captured on both hafnia and magnesia surfaces. Both oxide surfaces behaved similarly to alumina and exhibited a decrease in hydroxyl features (3200 to 3700 cm^{-1}) during the initial MoF_6 exposures. Additionally, $MoOF_4$ peaks were observed after the first MoF_6 pulse for both hafnia and magnesia. Lastly, MoO_x bands were identified for the hafnia and magnesia surfaces in the rage of 1010-810 cm^{-1} and 980-810 cm^{-1}, respectively. From these data, it is evident that these metal oxides undergo similar surface reactions. The interfaces at these oxides appear to consist of metal-fluoride and molybdenum oxyfluoride species during the early stages of MoS_2 ALD. Prior DFT studies for these metal oxides indicate the formation of MoO_x bonds[37], and our experimental observations are consistent with these computation results. See supplementary material at [URL will be inserted by AIP Publishing] for *in situ* FTIR data for hafnia and magnesia.

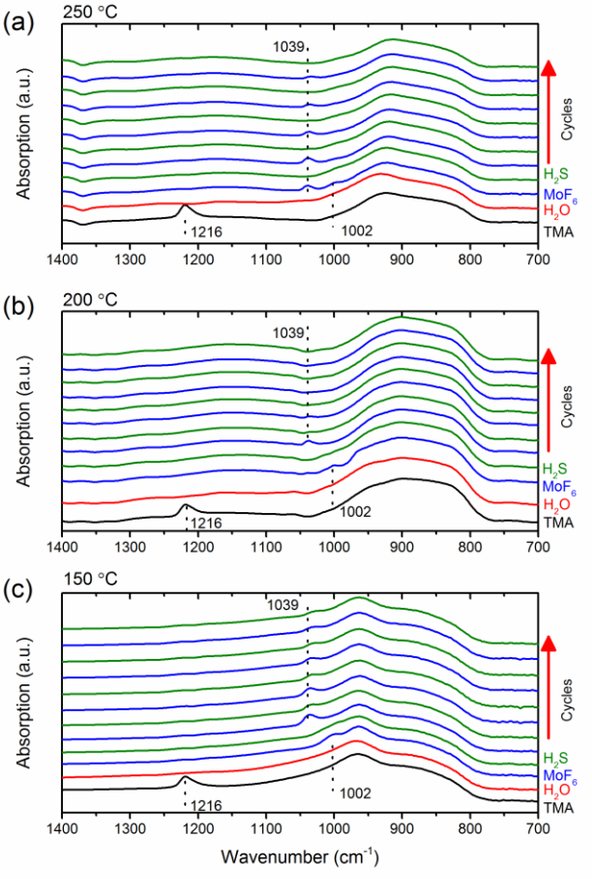

FIGURE 3. *In situ* FTIR absorption measurements at (a) 150, (b) 200, and (c) 250 ºC. In each, the first two spectra, in red and black, are the final TMA and H_2O ALD half-cycles. Subsequent cycle precursor and number are labeled to the right of the axes. As indicated by the labels and dashed lines, peaks appear at ~1039 cm^{-1} following exposure to MoF_6, which we assign to the formation of $MoOF_4$ following Ref. 38 and 39. Spectra are offset for clarity.

3. Ex situ XPS Measurements, Part 1

Ex situ X-ray photoelectron spectroscopy was used to investigate initial chemical bond formation from the first surface reactions. Each of the metal oxide surfaces was subjected to a single dose of MoF_6, after which the samples were briefly exposed to air and then transported to the XPS system in a sealed container. See supplementary material at [URL will be inserted by AIP Publishing] for XPS survey spectra of each metal oxide. Figures 4(a-c) show the resulting high resolution XPS scans of the F 1s region for each metal oxide. On each metal oxide surface, the F 1s spectrum is dominated by F bound to the metal from the underlying substrate. This result signifies that the MoF_6 precursor dissociated upon contact with the metal oxide surface to form the corresponding metal fluoride. In each case, a lower concentration of Mo-F bonding can be found at the lower binding energies as well as adventitious C-F bonds from the brief air exposure during transfer or residual C from metal oxide surfaces.

High resolution scans were additionally acquired for the Mo 3d region of each metal oxide surface following MoF_6 exposure (Fig. 4(d-f)). Deconvolution of the Mo 3d region revealed MoO_3 bonding with Mo $3d_{5/2}$ and Mo $3d_{3/2}$ peak doublets at ~232.3 eV and ~235.5 eV, respectively. A peak separation of 3.13 eV is found between Mo $3d_{5/2}$ and Mo $3d_{3/2}$, consistent with literature for the Mo^{6+} assignment[45, 46]. On the alumina surface, an additional doublet was found at 234.8 eV. We tentatively assign this doublet to $MoOF_4$ bonding. Overall, the XPS

results are consistent with FTIR observations for the first MoF_6 exposure on the metal oxide surfaces.

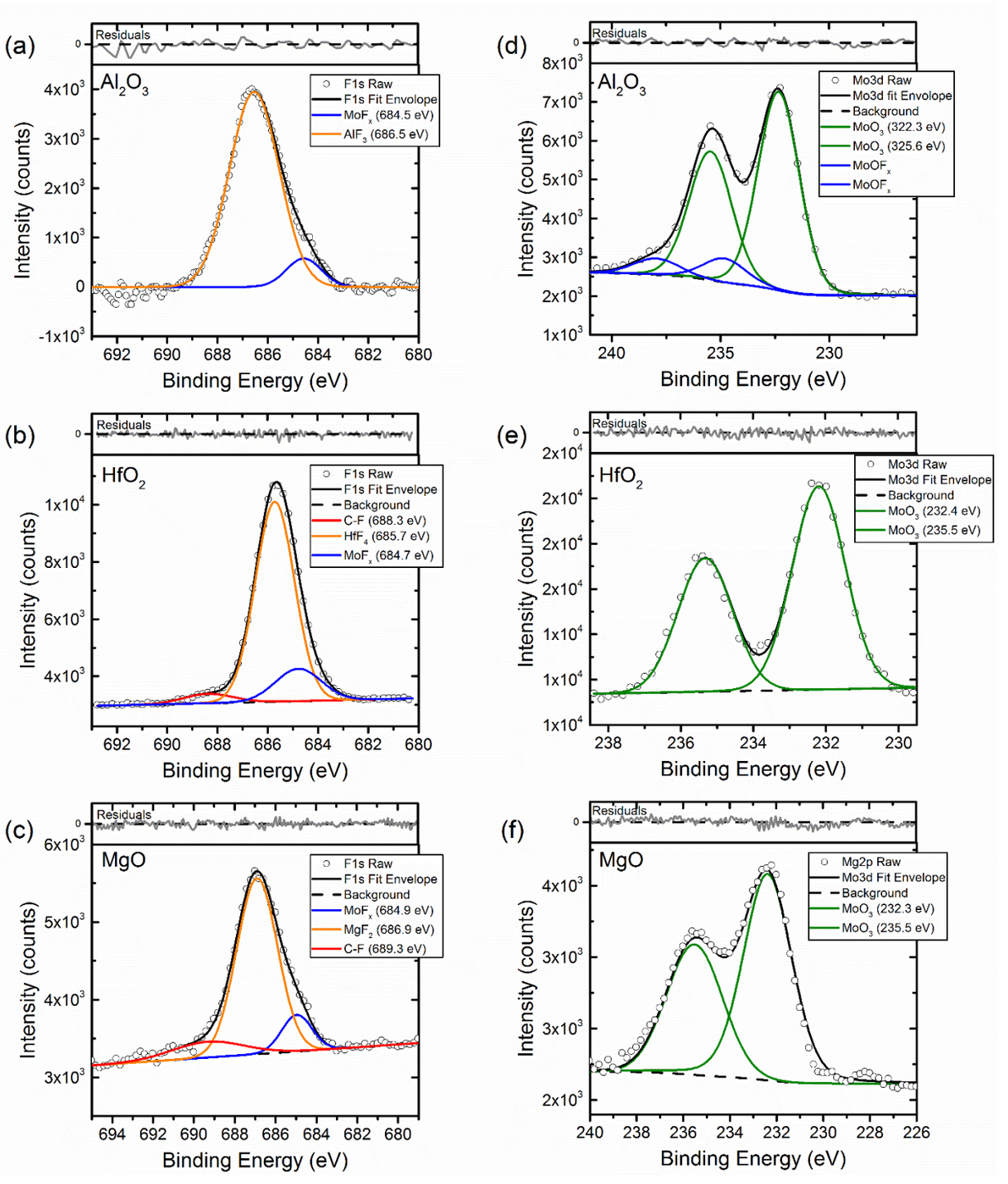

FIGURE 4. High resolution XPS scans of F 1s on (a) alumina, (b) hafnia, (c) magnesia and Mo 3d peaks on (d) alumina, (e) hafnia, (f) magnesia after a single MoF_6 dose on metal oxide surfaces at 200 ºC. Peak fitting reveals metal fluoride bonding is favorable on each metal oxide substrate as well as MoO_3 bonding.

4. Density Functional Theory Modeling of MoS_2 Nucleation

To further understand the surface reactions during the first MoF_6 pulse, first-principles density functional theory (DFT) simulations were employed. Previously, we employed DFT simulations to understand the reactions of a single MoF_6 with alumina, hafnia, and magnesia surfaces[37].That study supported the important role of surface hydroxyl groups in changing the surface electron density and promoting the dissociation of MoF_6. Extending that work to gain further insight into the nucleation reactions, here we included additional MoF_6 molecules to study cooperative effects[47]. Up to three MoF_6 precursors were introduced above the 2×2×1 supercell surface one at a time followed by a full geometry optimization after the addition of each precursor. Five hydroxyl (OH) groups were placed on the same 2×2×1 supercell surface to approximate experimental conditions at 200 ºC. We note that these DFT studies were performed on crystalline alumina surfaces, while the experimental results are for MoF_6 nucleation on amorphous alumina. While these surfaces are structurally quite different, we expect the bonding behavior to be similar for the two systems. Future DFT studies with disordered alumina could be performed to determine the relative contributions of surface structures on MoF_6 nucleation.

Images of the relaxed systems containing two and three MoF_6 above the alumina substrate were acquired to understand how the precursors would react with the surface. The charge density difference ρ_{diff} was calculated by taking the charge density of the optimized

MoF_6/alumina system $\rho_{total\ system}$ and subtracting the individual charge density contributions of the surface $\rho_{surface}$ and MoF_6 precursor ρ_{MoF_6}:

$$\rho_{diff} = \rho_{total\ system} - \rho_{surface} - \rho_{MoF_6}$$

The resulting figures reveal the residual charge densities resulting from the electrons participating in adsorption. Figures 5 and 6 show the images of the alumina surface with two and three MoF_6 precursors, respectively, after a full geometry optimization as well as the charge density difference. In Figure 5(a) the two MoF_6 precursors demonstrate different types of adsorption and are labeled "1" and "2" in the image. MoF_6 precursor 1 remains relatively intact with some slight bond angle and length distortion, and the bottom F atoms on precursor 2 bond to two different surface Al atoms. Precursor 2 reacts with the surface differently. Two F atoms from the precursor 2 subsequently disassociate and bond to a surface Al atom away from the precursor. The change in charge on the remaining MoF_5 molecule appears to promote a Mo-O bond at the surface, which agrees well with our FTIR and XPS measurements. Figure 5(b) illustrates the chemical bonding occurring at the surface by calculating the charge density difference. Cyan and yellow isosurfaces represent a gain and loss of electron density, respectively. Blue surfaces in the images indicate the end of the unit cell. Note that the orange regions are a product of O atoms (red) overlapping with a yellow isosurface, and do not indicate a different type of isosurface. Cyan isosurfaces between the Mo-O and Al-F atoms indicate chemisorption between the two MoF_6 precursors and the alumina surface[37]. Chemisorption occurs when electrons participate in bonding between atoms, and Figure 5(b) demonstrates this with the locations of the cyan isosurfaces.

Figure 6(a) contains an image of the alumina surface after a third MoF_6 precursor is introduced. Again, the precursors are numbered 1, 2, and now 3 for clarity. The third precursor

appears to dissociate upon interaction with the surface by the removal of a F atom, and subsequent Al-F bond formation. The additional F atoms on the surface facilitate Al bridging by means of the F atoms. Precursor 2 creates an $MoOF_4$ complex, which we calculated as having a negative change in free energy in our HSC Chemistry calculations (see section 3.1.5 below). Although the calculated $MoOF_4$ complex shares an F atom with precursor 1, the formation of an $MoOF_4$ complex is identified in the FTIR data (see section 3.2.2 below). An AlF_3 forms with the dissociated F atoms from three precursors. Precursor 3 has some slight bond angle and length distortion, but similar to precursor 1 in Fig. 5, it remains intact aside from the loss of a F atom, and these distortions can be considered negligible. The charge density difference calculations in Figure 6b reveal a change in surface chemistry. Similar to Fig. 5(b), there is the formation of Mo-O and Al-F bonds between the precursors and surface. Also, the cyan isosurfaces surrounding the Mo atoms of the precursors expands across the surface. These results reveal interactions between adsorbed precursors during the first half-cycle of MoF_6. Overall, the DFT calculations support the FTIR and XPS measurements by identifying Mo-O bonds and Al-F bond formation. These results provide further insight into the metal-oxygen-fluoride character of the interface between the MoS_2 and substrate oxide.

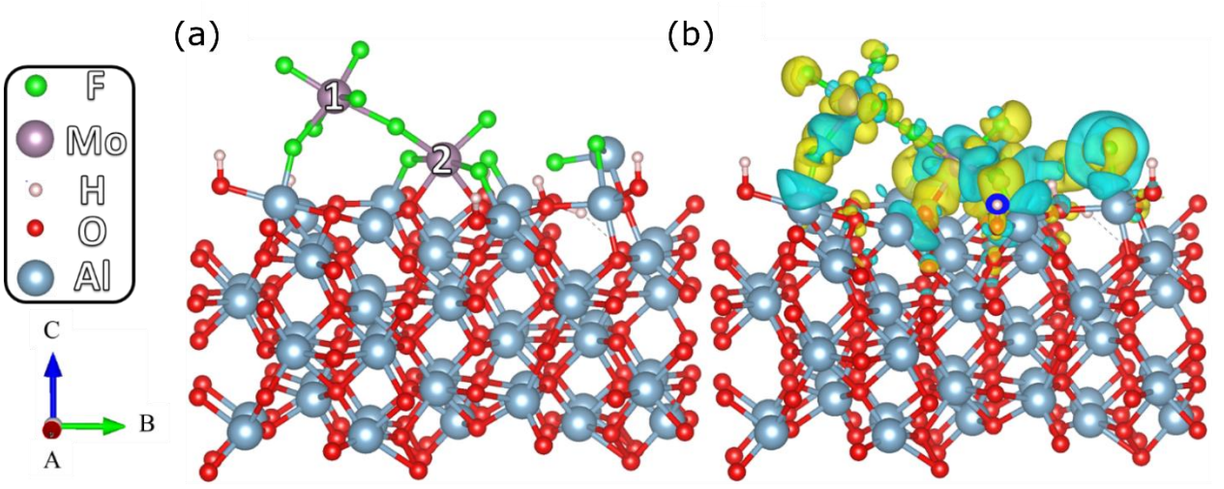

FIGURE 5. Atomic models resulting from density functional theory (DFT) simulations of the relaxed system (a) and charge density difference (b) of an alumina surface with two MoF_6 precursors. The MoF_6 precursors are numbered 1 and 2 to help distinguish how each reacts with the surface. Cyan and yellow isosurfaces indicate a gain or loss of electrons, respectively. Precursor 1 shows MoF_x-O formation. Fluorine atoms from precursor 2 are shown bonding to Al atoms indicating favorable Al-F bonding.

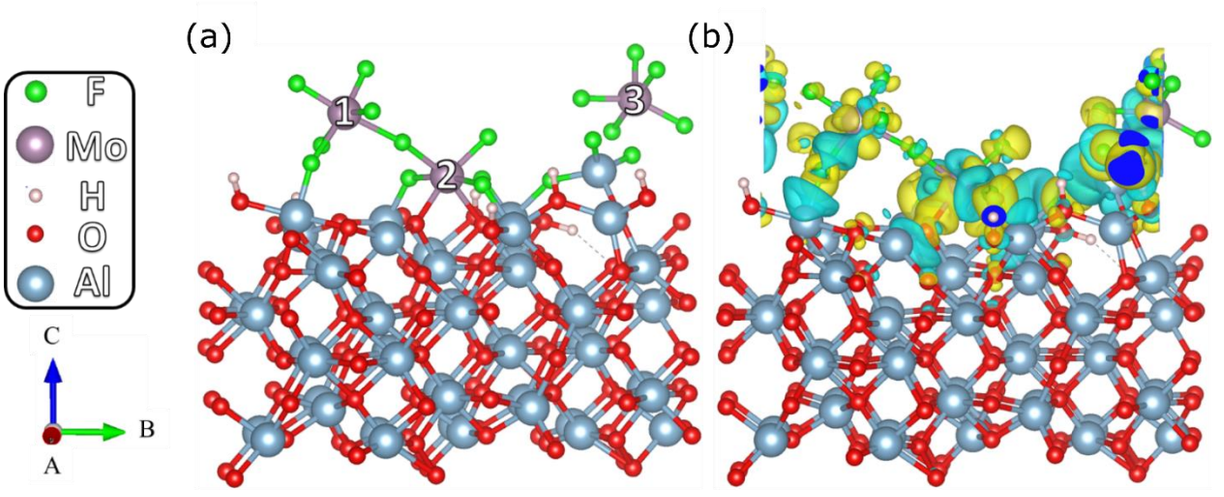

FIGURE 6. DFT atomic models of the relaxed system (a) and charge density difference (b) of an alumina surface with three MoF_6 precursors. The MoF_6 precursors are numbered 1, 2, and 3 to help distinguish how each reacts with the surface. Cyan and yellow isosurfaces indicate a gain or loss of electrons, respectively. The addition of a third MoF_6 promotes both AlF_3 and $MoOF_4$ bonds.

5. RGA of first MoS_2 ALD cycle

Residual gas analysis of the reaction chamber was performed during MoS_2 ALD on an alumina surface. Chemical byproducts were studied to gain a better understanding of the reactions that take place during the first and second half-cycles. A multi-pulse dosing scheme of AAAAAA-BBBBBB… was performed, where A is a MoF_6 pulse, B is a H_2S pulse, and a purge

is used after each precursor pulse. This pulsing scheme allows for separation of byproducts from precursor fragments and background gasses. The RGA intensities for H_2O (m/e = 18), HF (m/e = 20), and F_2 (m/e = 38) are shown in Figure 7. Black and grey vertical dashed lines indicate the first pulse of MoF_6 and H_2S, respectively.

An increase in the H_2O and HF intensity is observed following the initial MoF_6 exposure. Successive pulses of MoF_6 show little to no response from H_2O species indicating that this is a potential byproduct from the first half-cycle and can be attributed to the release of the surface hydroxyl groups. The initial HF peak does show a slight difference in pressure compared to the successive pulses indicating some F is released from the MoF_6 precursor during the reaction with the surface. These results are supported by the FTIR data, which indicated the consumption of hydroxyl groups upon exposure to MoF_6. The second half-cycle shows that substantial amounts of H_2O and HF byproducts are produced from the reaction of H_2S with the previously formed surface. It is clear from the decrease in HF intensity, with subsequent pulses, that the species is indeed a byproduct of the reaction. The decrease in intensity indicates a reduction in byproduct formation as the substrate surface reactions saturate. The observed H_2O intensity does not significantly change during the successive H_2S dosing. This indicates that H_2O could be a part of the background gasses formed during the H_2S pulse. However, from the reaction equations discussed below, it is thermodynamically favorable that H_2O is a byproduct of the second half-cycle reaction, but this result cannot be differentiated by the gas analysis. Further experimentation is required to confirm this species. During both half-cycles, the F_2 concentration is negligible compared to the two primary gaseous species. These observations inform the hypothesized reaction equations discussed below.

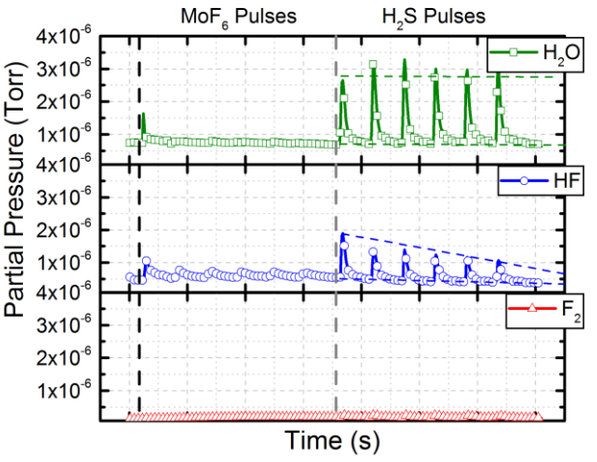

FIGURE 7. Residual gas analysis intensities for H_2O (m/e = 18), HF (m/e = 20), and F_2 (m/e = 38) during the first cycle of MoS_2 ALD on alumina at 200 ºC. Gaseous H_2O was the primary byproducts observed after during the first MoF_6 exposure. HF and possibly H_2O can be observed as byproducts from the H_2S reaction. Vertical black dashed line indicates beginning of MoF_6 pulses and the grey vertical dashed line indicates beginning of H_2S dosing. Six consecutive doses of each precursor were conducted during experiment.

6. Nucleation Reactions

With the above insights into nucleation, we can hypothesize the surface reactions and byproducts from for the first ALD half-cycle. In the following analysis, we will use the thermodynamics of bulk chemical transformations to evaluate potential surface chemical pathways for the ALD half-reactions. We start by considering a few possible reactions between MoF_6 and alumina as listed in Table 1.

TABLE 1. Reaction equations representative of the MoF_6 half-reaction on Al2O3.

$Al_2O_3 + MoF_6(g) \rightarrow 2AlF_3 + MoO_3;\ \Delta G = -442\ \frac{kJ}{mol\ Mo}$	Eq. 2
$Al_2O_3 + 3MoF_6(g) \rightarrow 2AlF_3 + 3MoOF_4;\ \Delta G = -186\ \frac{kJ}{mol\ Mo}$	Eq. 3

$Al(OH)_3 + MoF_6(g) \rightarrow AlF_3 + 3MoO_3 + 3HF(g);\ \Delta G = -357 \frac{kJ}{mol\ Mo}$	Eq. 4
$Al(OH)_3 + 3MoF_6(g) \rightarrow AlF_3 + 3MoOF_4 + 3HF(g);\ \Delta G = -158 \frac{kJ}{mol\ Mo}$	Eq. 5
$2Al(OH)_3 \rightarrow Al_2O_3 + H_2O(g);\ \Delta G = -35 \frac{kJ}{mol\ Al}$	Eq. 6

The changes in Gibbs free energy, ΔG, are calculated for the above equations at 200 ºC using HSC Chemistry[48]. All equations shown are energetically favorable, with a large, negative Gibbs free energy. Formation of aluminum fluoride is common to all equations showing the substrate interaction with MoF_6 precursor. We have included reaction equations that consider both non-hydroxylated (Eq. 2 and Eq. 3) and hydroxylated (Eq. 4 and Eq. 5) alumina. These equations show favorability of both Al-F bonding and MoO_3 (Eq. 2) and $MoOF_4$ (Eq.3) species. The hydroxylated alumina equations provide support for the gaseous byproducts that are seen in RGA analysis. Equations (4) and (5) demonstrate the favorable formation of HF gas. Equation 6 shows the favorability of the hydroxyl groups forming H_2O at 200 °C. The combination of these reaction equations can help describe the gaseous byproducts seen in RGA, possibly indicating that MoF_6 facilitates the removal of hydroxyls to form HF. MoO_3 (Eqs. 2 and 4) and $MoOF_4$ (Eqs. 3 and 5) are both viable products although MoO_3 formation is substantially more favorable. XPS measurements following MoF_6 exposure to the alumina surface reveal both MoO_3 and $MoOF_4$. The large free energy change of -442 kJ/mol for Eq. 3 is not unexpected as Mo readily oxidizes even at relatively low temperatures[49] and AlF_3 is extremely stable. Previous reports have also found metal oxyfluoride species when metal oxides are exposed to fluoride compounds[38]. See supplementary material at [URL will be inserted by AIP Publishing] for reaction equation calculations on both magnesia and hafnia. We note that the ordering of free

energy changes for MoF_6 reaction with these metal oxides ($MgO < Al_2O_3 < HfO_2$) reflects the relative stability of the fluorides compared to their corresponding oxides.

TABLE 2. Reaction representative of the H_2S half reaction on Al2O3.

$MoO_3 + 3H_2S(g) \rightarrow MoS_2 + 3H_2O(g) + S;\ \Delta G = -180\ \frac{kJ}{mol}$	Eq. 7
$MoOF_4 + 3H_2S(g) \rightarrow MoS_2 + 4HF(g) + H_2O(g) + S;\ \Delta G = -318\ \frac{kJ}{mol}$	Eq. 8

Reaction equations representative of the second half-cycle on the alumina surface can be found in Table 2. These equations show the favorable formation of MoS_2 species when either MoO_3 or $MoOF_4$ are exposed to the H_2S precursor. The byproducts can become quite complicated, and require additional study, but do show gaseous H_2O and HF (Eq. 8), which can be supported by the RGA data (Fig. 7). The reaction equations also contain S byproducts in both Eq. 7 and Eq. 8. Elemental sulfur could desorb as a volatile byproduct, as mentioned previously[50], or could incorporate into the films to form sulfur-ion clusters[29].

These proposed surface reactions suggest that the reaction of MoF_6 with metal oxides to produce Mo-oxide and metal-fluoride species is thermodynamically favorable. Thermodynamic calculations indicate that the reactions of these species with H_2S are energetically favorable for the formation of MoS_2 with the byproducts observed by RGA. Based on these results, the nucleation of MoS_2 on metal oxides begins during the first ALD cycle with MoF_6 and H_2S. Understanding the transition from the nucleation reactions of Eq. 1-5 to the steady-state growth described by Mane *et al.* requires additional study.

B. Transition to Steady-State Growth

1. In situ QCM Measurements, Part 2

With a better understanding of the hetero-nucleation reactions, insight into the transition to steady-state growth can be gained by examining the subsequent MoS_2 ALD cycles on the oxide surfaces with QCM. Plotting the mass change per cycle (MCPC) of MoS_2 in Figure 8, the first MoS_2 ALD cycle on Al_2O_3 shows a much larger mass increase compared to the subsequent cycles. From DFT and XPS, we can conclude that this large mass gain results from conversion of the Al_2O_3 substrate to AlF_3 and a higher density of adsorbed Mo and S compared to subsequent cycles due to the large number of Al-OH binding sites. As supported by DFT and RGA, very little gaseous byproduct is formed during the first half-cycle, thus retaining much of the added mass from the MoF_6 precursor. The second cycle of MoS_2 then shows a mass decrease at 200 and 250 ºC, indicating a release of volatile surface species. With subsequent MoS_2 ALD cycles a "hump" in the data is observed on the alumina surface. This hump can be caused by island coalescence, providing more surface area for precursor reactions. Similar results can be identified in the hafnia and magnesia surfaces at lower deposition temperatures (SI Fig. S2). Puurunen *et al.* developed a phenomenological model to describe islanding on a surface[51] and would suggest that substrate-inhibited growth (Type 2) is occurring. It should be noted that the lower growth temperatures indicate steady state deposition is achieved in fewer cycles in Fig. 8, which can be attributed to a higher concentration of hydroxyl groups that serve as seeds to create the islands. The increased hydroxyl coverages increase the MoF_6 nucleation density, resulting in fewer cycles to achieve coalescence. The steady state MoS_2 MCPC is slightly dependent on growth temperature. For deposition on alumina, the MoS_2 MCPC increases from ~16 ng/cm^2 at 150 ºC to ~19 ng/cm^2 at 200 ºC and ~21 ng/cm^2 at 250 ºC.

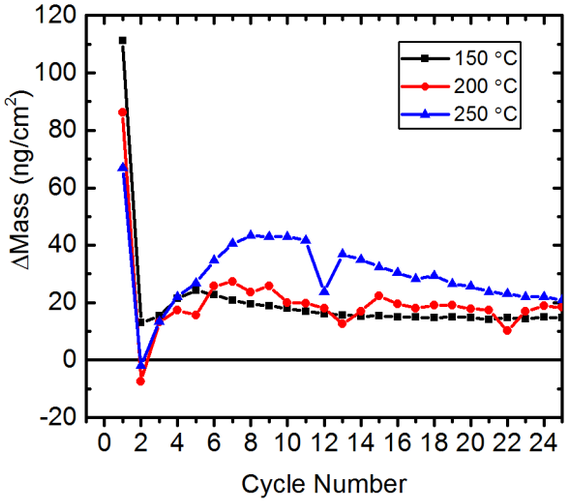

FIGURE 8. Mass change per cycle for MoS_2 deposition at 150, 200, and 250 ºC on ALD alumina. Islanding formation and coalescence behavior is observed for each growth temperature.

Both magnesia and hafnia show similar trends, where the 150 ºC deposition temperature shows islanding growth behavior (see Figure S2). The 250 ºC deposition temperature shows more of a substrate enhanced growth behavior for both magnesia and hafnia oxides[51]. Lastly, steady deposition behavior for magnesia and hafnia varied slightly with temperature. As seen in Figure S2(a), hafnia showed an inverse temperature dependence where 150 ºC gave the largest MCPC and 200 ºC gave the lowest. Magnesia, Figure S2(b), showed the same MCPC for both 150 ºC and 250 ºC. At a growth temperature of 200 ºC, there was slightly higher steady state deposition rate than at the other temperatures. See supplementary material at [URL will be inserted by AIP Publishing] for additional details and discussion..

2. In situ Fourier Transform Infrared Measurements, Part 2

In situ FTIR spectra in Figure 9 show data from MoS_2 ALD cycles 1, 2, 4, and 8 on alumina. After the first MoF_6 pulse (blue), the oxide bulk modes in the range of ~800-1200 cm^{-1}

decrease. After the second cycle, peak emergence at 1039 cm^{-1} was associated with $MoOF_4$ formation. A wide metal oxide band can be observed for frequencies below the $MoOF_4$ mode. As discussed previously, MoO_x species have been experimentally verified and found in the range of 995-820 cm^{-1} on alumina. MoO_x bond formation is further supported by density functional theory calculations and XPS measurements, as discussed above. As the MoS_2 ALD continues, changes in the MoO_x region diminish indicating that MoO_x bonds are no longer participating in the surface chemistry and the surface has converted to MoS_2. This can be more clearly seen in the 8th and final cycle in the plot, with very few narrow modes present in the difference spectra.

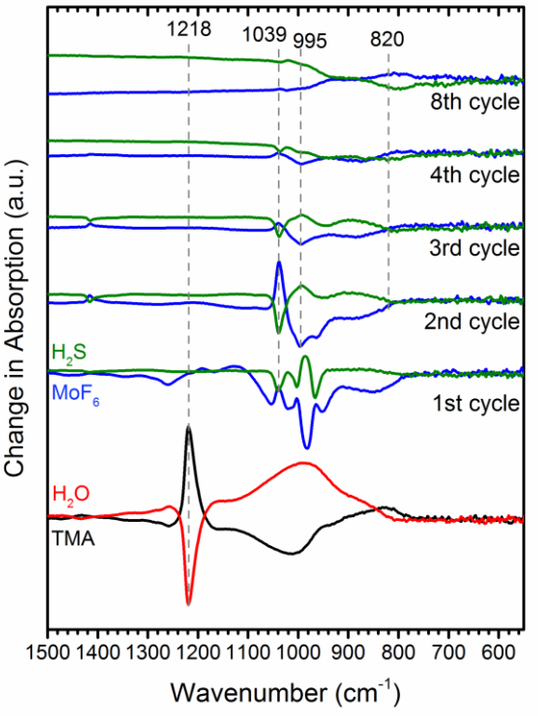

FIGURE 9. *In situ* FTIR difference spectra of alumina after the first few MoS_2 cycles at 200 ºC. Plot range limited to 550-1500 cm^{-1} for clarity of peak mode detection. Key modes are labeled. Black and red difference spectra is from the last ALD cycle of substrate oxide. Blue and green spectra denote MoF_6 and H_2S dosing, respectively. Spectra are offset for clarity.

With further MoS_2 ALD cycles, we observed a progressive increase in the FTIR baseline signal. See supplementary material at [URL will be inserted by AIP Publishing] for raw absorption spectra on alumina. We attribute this baseline increase to absorption by free carriers in the MoS_2 semiconductor. To quantify these changes, we calculated the average intensity value from a featureless region between 1675 to 1725 cm^{-1} and plotted this versus MoS_2 ALD cycle number for each temperature in Figure 10. For reference, we included the average baseline values for the final TMA and H_2O cycles of the alumina ALD in these plots. Little change to the baseline was observed for approximately six MoS_2 ALD cycles for all growth temperatures. After this incubation period, the baseline increases approximately linearly with MoS_2 ALD cycles, and we attribute this increase to the growth of MoS_2. Superimposed on this linear baseline increase the signals are observed to oscillate. The signals decrease during MoF_6 exposures and increase during the H_2S exposures suggesting that the film becomes more conductive during the H_2S pulses. These results indicate a transition to bulk-like behavior after as few as five cycles. This transition to a linearly increasing baseline and distinct signal oscillations correlates well with the loss of the $MoOF_4$ peak at all temperatures. For instance, the peak at 1039 cm^{-1} disappears after about 5-6 cycles in Figure 3, roughly coincident with transition in Figure 10. This suggests that once the reactions stop consuming oxygen, Mo-S bonds start to form. See supplementary material at [URL will be inserted by AIP Publishing] for raw absorption FTIR spectra for deposition on hafnia and magnesia. The absorption increased significantly for hafnia and magnesia, but similar transitions were observed after roughly 5-8 cycles.

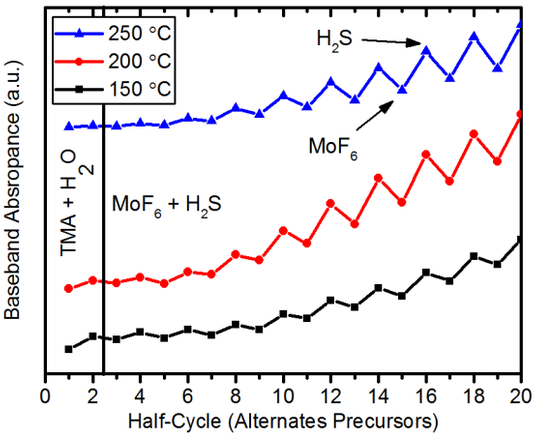

FIGURE 10. *In situ* FTIR absorbance for 10 cycles of MoS_2 on alumina. The absorbance was determined by the y-intercept of a horizontal line fit to 1725 to 1675 cm^{-1} region of the FTIR spectra at each temperature. Each data point represents a single half cycle. For reference, baseline data are included for the final TMA and H_2O exposures for the alumina ALD.

3. *Ex situ XPS Measurements, Part 2*

To gain better insight of the chemical bonding after multiple cycles of MoS_2 ALD, XPS survey scans were acquired. Samples were prepared using 50 MoS_2 ALD cycles on alumina-coated Si coupons at 150, 200, and 250 ºC. See supplementary material at [URL will be inserted by AIP Publishing] for the XPS survey spectra. Survey scans showed C, O, F, Al, S and Mo content. Their elemental atomic concentrations are provided in Table 2. Fluorine was detected for each deposition temperature. From Table 3, the Mo and S percentages increase while the O and F concentrations decreases with deposition temperature. We calculate S/Mo ratios of 0.98, 1.09, and 1.53 for deposition temperatures of 150, 200 and 250 ºC, respectively. These atomic percentages do not indicate stoichiometric MoS_2 films, but rather a mix of MoS_x and MoO_xS_y species. With the thickness of these films being less than the maximum photoelectron escape depth, we expect XPS spectra to contain contributions from surface oxides as well as any

potential oxidation that occurred during sample transfer. Thus, while the insights to nucleation and growth reported here may be valuable for thermal ALD with the MoF_6 and H_2S chemistry, they may not apply to other ALD processes that produce stoichiometric MoS_2 films.

TABLE 3. Atomic percentages from XPS survey scans after 50 cycles of as-deposited MoS_2 ALD on alumina.

Sample	C 1s	O 1s	F 1s	Al 2p	S 2p	Mo 3d
150 ºC	6.57	26.25	9.85	39.68	8.75	8.9
200 ºC	6.97	21.4	9.79	37.23	12.85	11.76
250 ºC	0.31	5.93	6.71	1.65	51.78	33.63

High resolution XPS measurements of the Mo 3d and S 2p regions of the as-deposited films on alumina are shown in Figure 11. Deconvolution of the Mo 3d region, in Figure 11(a), shows MoS_2, MoO_2, and MoO_3 species at all growth temperatures. The primary MoS_2 doublet for Mo^{4+} oxidation was found at ~229.5 eV. MoO_2 species were identified by the Mo $3d_{5/2}$ doublet located at binding energies of ~230 eV. Lastly the MoO_3 doublet could be found at binding energy of ~232 eV. These peak locations have been reported for the Mo^{5+} and Mo^{6+} oxidation states, respectively[52, 53]. Interestingly, at 150 ºC deposition temperature there was an intermediate doublet found at ~228 eV, which was attributed to a MoS_x species.

As the deposition temperature increased, there was a resulting decrease in both the MoO_2 and MoO_3 peaks. This can be seen clearly by the decrease in the shouldering of the Mo $3d_{3/2}$ peak located at ~235 eV for MoO_3 species. Unsurprisingly, the stability and presence of MoO_3 and MoO_2 species[52] can contribute to the impediment of MoS_2 formation at the lower temperatures,

producing the lack of stoichiometric MoS_2. Values for the atomic percentages of the peak fits can be found listed in Table 4.

TABLE 4. Atomic percentages from XPS high-resolution scans of as-deposited 50 cycles MoS_2 ALD on alumina.

	150 °C		200 °C		250 °C	
Atomic %	Mo 3d	S 2s	Mo 3d	S 2s	Mo 3d	S 2s
MoS_2	5.61	44.9	19.56	66.24	31.12	74.92
MoO_x	83.27		63.45		51.4	
MoO_xS_y	8.92		7.8		1.4	
S_x		55.11		33.77		25.08

Figure 11(b) shows high resolution scans of the S 2p region, which gives more insight into bonding within the films. All deposition temperatures showed two sulfur oxidation doublets present. The S $2p_{3/2}$ peak for S^{2-} was located at ~162 eV, an oxidation state of sulfur found for MoS_2 [53, 54]. Interestingly, a higher energy doublet at ~164 eV was found. This binding energy is typically associated with elemental sulfur. However, it has been reported that upon sulfurization of MoO_3 films by H_2S, between temperatures of 150-200 ºC, no elemental sulfur remains in the films[55]. This suggests that this doublet peak could be due to poly-sulfide ion clusters, as previously found in the evolution of these MoS_2 films[29] or an molybdenum oxysulfide species[53]. As the deposition temperature increased, we observe a decrease in these peaks with an inverted trend in the MoS_2 peaks. These results again suggest that with more thermal energy there are fewer poly-sulfide ions clusters forming and more MoS_2.

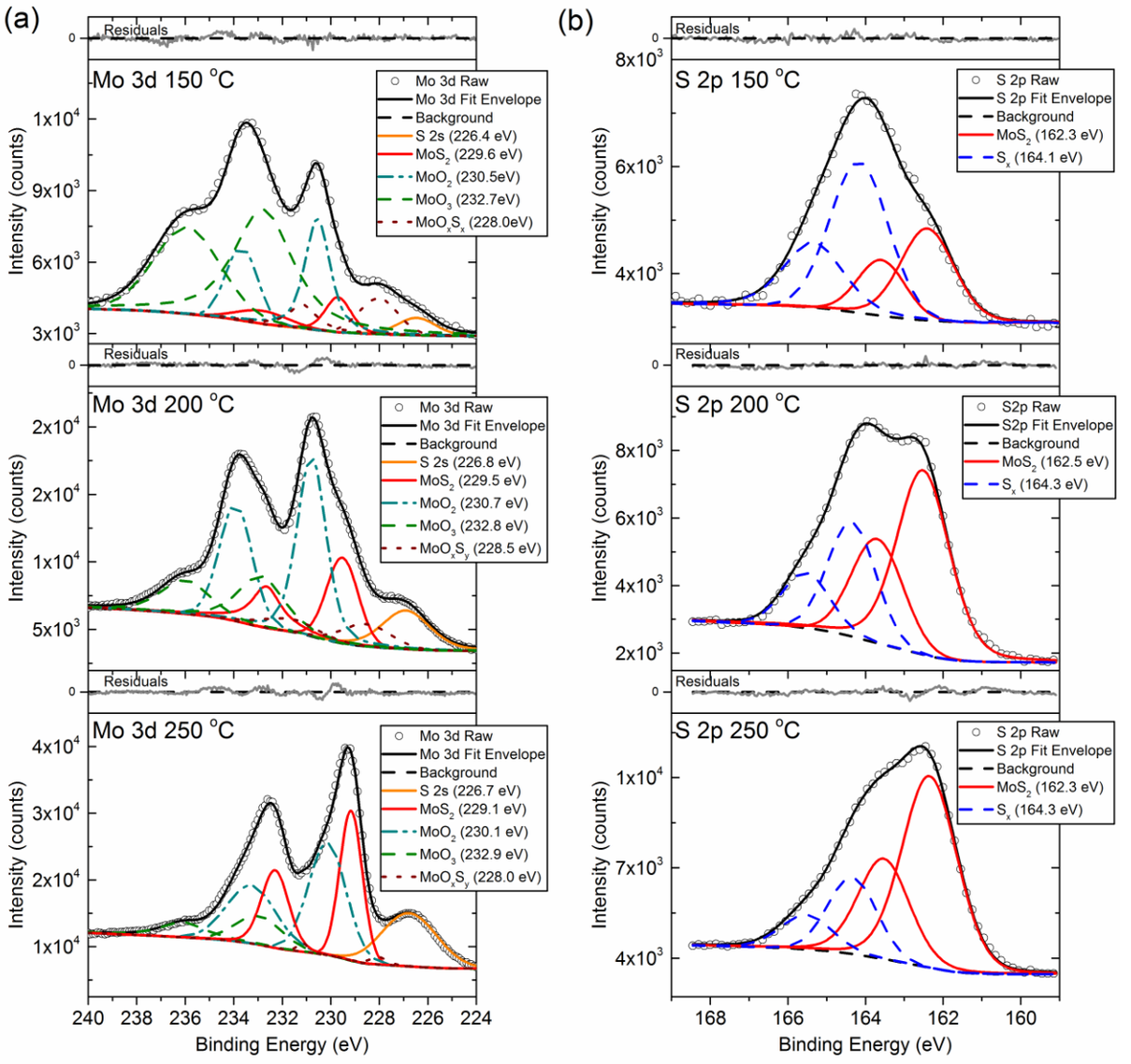

FIGURE 11. High resolution XPS spectra of the (a) Mo 3d and (b) S 2p regions of 50 cycles of as-deposited MoS_2 on ~20 nm ALD alumina at 150, 200, and 250 ºC. A decrease in the MoO_x peaks can be seen as the deposition temperature increased. This decrease in MoO_x is coupled with the increase in the MoS_2 bonding.

4. Ex-Situ Thickness measurements

Spectroscopic ellipsometry (SE) measurements were performed on as-deposited and annealed films to determine MoS_2 film thickness. Samples were prepared by 50 MoS_2 ALD cycles on alumina and hafnia coated Si coupons at 160, 200, and 250 °C. Low mean squared error (MSE) values for SE models of films deposited on magnesia substrates could not be obtained, so data for deposition on magnesia were not included in further analysis. See supplementary material at [URL will be inserted by AIP Publishing] for additional details and SE data. Thickness data for 160 and 200 °C samples can be found in Figure 12. Thickness data for the 250 °C sample was excluded as the roughness of the films were on the same order as the measured thickness (this will be detailed further in the next section). A clear trend was found showing an increase in film thickness as the growth temperature was elevated. This thickness increase is supported by the observed temperature dependence in MGPC as shown in previous QCM measurements. The trend in data can also suggest that at 160 °C the precursors have lower reactivity than at the elevated temperatures. After annealing the samples in an H_2S environment at 600 °C, a decrease in film thickness was observed. This result is expected as a more ordered film is formed and the concentrations of both fluorine and oxygen drop upon annealing[50]. On alumina substrates, the films are reduced in thickness by roughly 40% after annealing. The hafnia samples showed a larger thickness decrease closer to 60% after annealing.

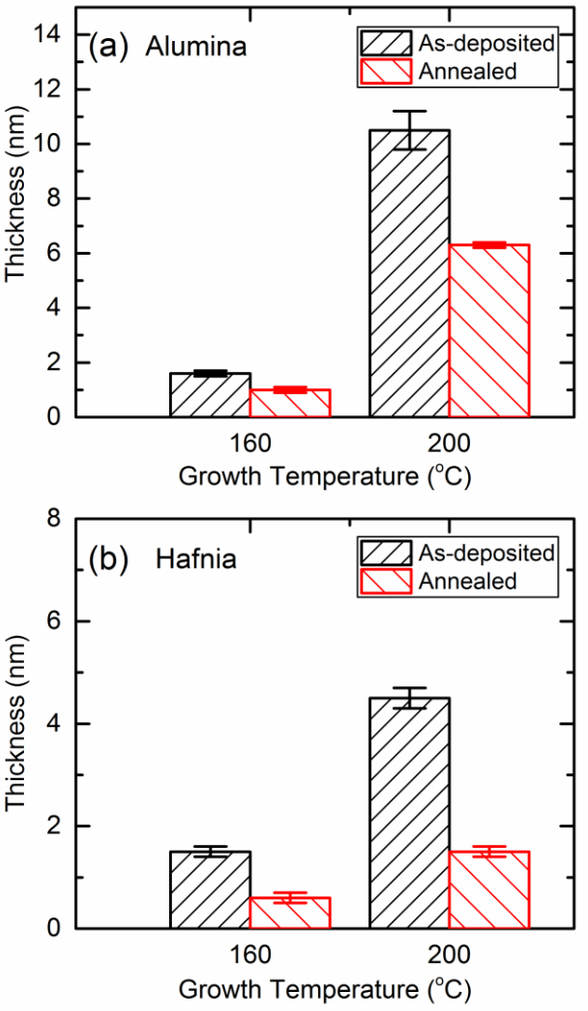

FIGURE 12. Film thickness measurements as measured by spectroscopic ellipsometry after 50 cycles of MoS_2 ALD on (a) alumina and (b) hafnia substrates. As-deposited films (black dashes) show an increase in thickness with growth temperature. The thickness of films is reduced after annealing (red dashes) in H_2S environment at 600 °C.

C. Crystalline MoS_2 Films

1. Ex situ morphology

To investigate the morphology of the films, Raman spectroscopy was used to look for crystalline MoS_2 modes for samples with 50 cycles of MoS_2 ALD. As described in previous

sections, the ALD MoS_2 films were amorphous as deposited and required annealing to crystallize. Interestingly, the as-deposited 50 cycle films grown at 250 °C showed crystalline MoS_2, while the films deposited at 160 and 200 °C, showed no crystalline characteristics. This was common on all growth substrates. See supplementary material at [URL will be inserted by AIP Publishing] for Raman spectroscopy measurements for as-deposited 200 and 250 °C films. Peaks at characteristic MoS_2 A_{1g} and E^1_{2g} modes can be identified for all 250 °C growth temperatures. Show in Figure 13, Raman spectroscopy measurements were taken on the alumina 250 °C sample before and after annealing in H_2S at 600 °C for 30 min. After annealing, the intensities of the modes are seen to increase and the FWHM of the E^1_{2g} peak decreases from 9.5 to 7.6 cm^{-1}. This result indicates an overall decrease in sulfur vacancy defects within the films[56, 57].

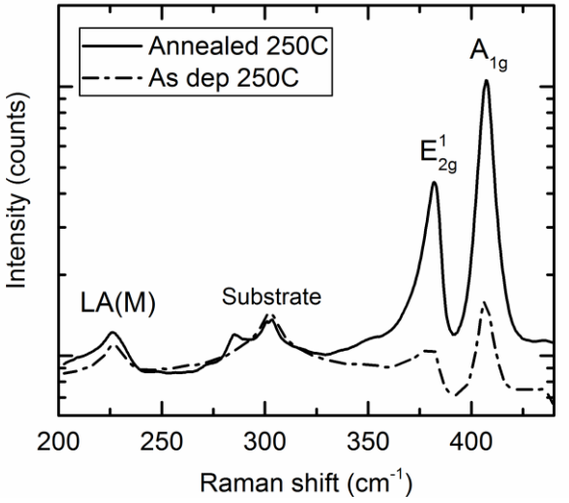

FIGURE 13. Raman spectroscopy scans of as-deposited (dashed line) and annealed (solid line) films after 50 cycles of MoS_2 ALD. An increase in intensity and decrease in FWHM of E^1_{2g} mode can be identified.

To gain more insight into the morphology of the as-deposited films, atomic force microscopy images (AFM) were acquired from as-deposited 200 and 250 °C samples. Figure 14 shows the topography results of the 250 °C samples. All samples deposited at 250 °C show high roughness, with an average Ra = 4.8 nm. This high roughness, along with the topography map indicate vertical flake formation. All 200 °C samples are much smoother in comparison due to the lack of crystallinity, where no vertical flakes could be identified. The flake formation is additionally supported by the previous Raman data of all sets of films, showing crystallinity of the 250 °C samples. See supplementary material at [URL will be inserted by AIP Publishing] for AFM images of the 200 °C MoS_2 films.

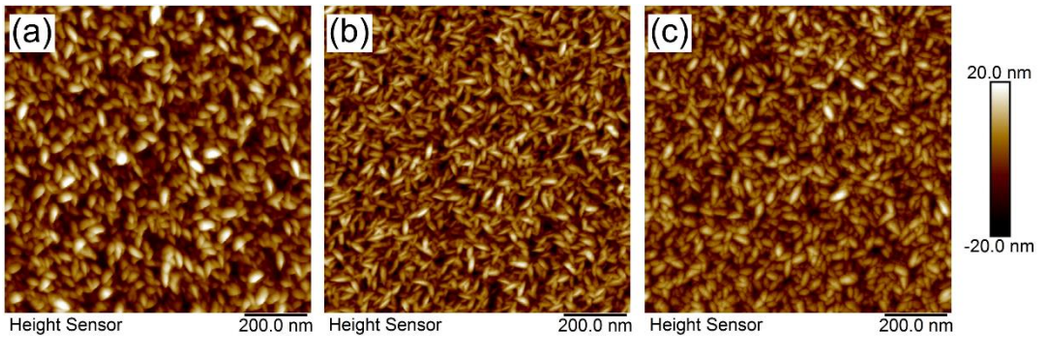

FIGURE 14. Atomic force microscope height images of as-deposited MoS_2 films grown with 50 cycles of ALD at 250 °C on (a) alumina, (b) hafnia, and (c) magnesia coated Si substrates. Topography results indicate the formation of vertical flakes for each surface.

To further look at the structure of the films, transmission electron microscopy (TEM) cross section images were acquired from films deposited with 50 cycles of MoS_2 on alumina at 200 °C and 250 °C. The film deposited at 200 °C was annealed at 600 °C for 30 min in H_2S. Both films were capped with an additional ALD alumina layer in preparation for FIB lift-out. Lift-outs were prepared as described in the experimental section. As expected, the annealed

sample exhibited a layered film with basal planes parallel to the growth substrate, as can be seen in Figure 15(a). As suggested by the AFM topography scans, TEM imaging shows vertical, flake like crystalline domains within the MoS_2 region on the as-deposited 250 °C sample. This can be seen in Figure 15(b), revealing basal planes orientated both vertically and horizontally to the substrate. This type of growth has been observed previously for plasma enhanced ALD growth of both MoS_2 and WS_2 [58, 59]. Spacing between MoS_2 layers was determined to be 0.65 ± 0.16 nm by conducting a Fast Fourier Transform (FFT) over the vertical flake region. This thickness is consistent with reported values[60]. We can rationalize the growth of vertical flakes as resulting from a higher reactivity of the ALD precursors on the edges of MoS_2 sheets as compared to the basal plane.

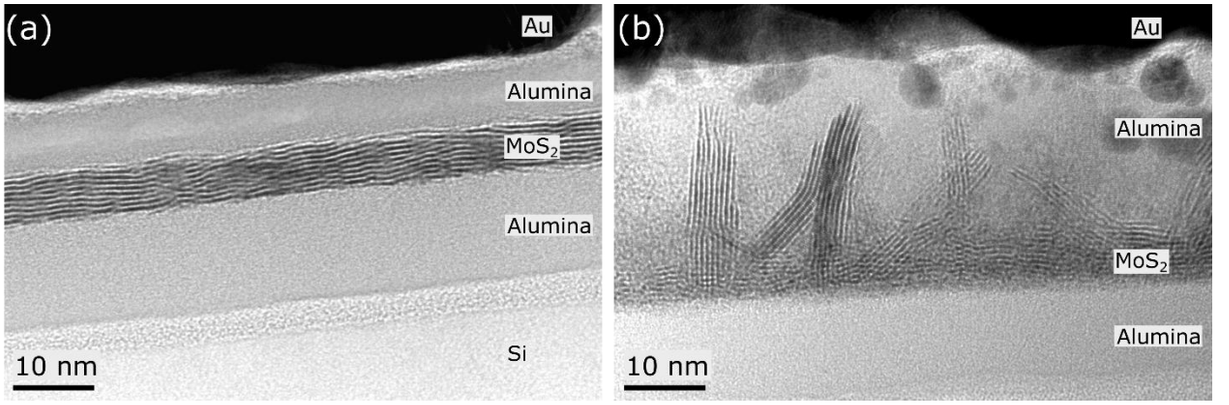

FIGURE 15. Transmission electron microscope cross section images of MoS_2 films (a) deposited at 200 °C, then annealed at 600 °C for 30 min in H_2S and (b) as-deposited films at 250 °C. Crystalline MoS_2 domains are parallel to growth substrate when deposition temperature is 200 °C, followed by annealing, while vertical flakes can be identified from as-deposited films grown at 250 °C.

2. Few layer MoS_2 films

Few-layer MoS_2 films were grown on planar coupons and MWCNTs. Few-layer films were achieved by two different ALD growth conditions. Films were grown at either 160 or 200 °C, with 50 or 22 MoS_2 ALD cycles, respectively. MoS_2 films were grown on each oxide substrate with both growth conditions. All films were annealed in H_2S at 600 °C for 30 min post deposition to induce a layered structure. Figure 16 shows Raman spectroscopy measurements of annealed films grown on alumina substrates for both growth conditions. Raman spectra revealed a ~23 cm^{-1} peak to peak distance between the A_{1g} and E^1_{2g} modes, which corresponds to three layers of a mechanically exfoliated film[61]. Additionally, plasma etching of CVD MoS_2 films down to 3.1 nm, or roughly 3-4 layers, gave a $A_{1g} - E^2_{1g}$ peak difference of 24.3 cm^{-1} [62]. Deposition on other oxide substrates yielded similar results, where other oxide substrates suggest few layer MoS_2 films. However, the 22 cycles of MoS_2 deposited at 200 °C on hafnia showed a larger peak separation of 26 cm^{-1}. This peak separation can indicate bulk MoS_2, however it is well known that sulfur defects can cause a shift in the E_{1g} peak to a lower wavenumber. It is possible there is a higher degree of defects within this film causing the observed increase in peak to peak distance. See supplementary material at [URL will be inserted by AIP Publishing] for the respective Raman data for deposition on hafnia and magnesia.

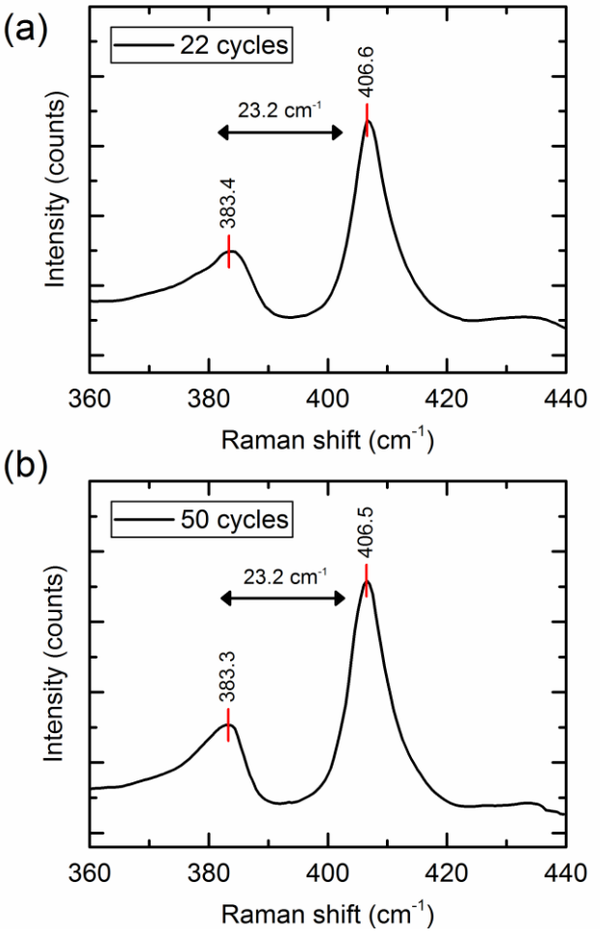

FIGURE 16. Raman spectra of MoS_2 thin films on alumina after (a) 22 cycles at 200 ºC and (b) 50 cycles at 160 ºC. Both films were annealed at 600 ºC in H_2S. Peak separation of 23 cm^{-1} between $A_{1g} - E^1_{2g}$ corresponds to a three-layer MoS_2 film.

To confirm layering of the MoS_2 films, deposition was performed on OH-functionalized multi-walled carbon nanotubes (MWCNTs) to facilitate imaging by TEM. OH- functionalized carbon nanotubes were first coated with ALD alumina prior to MoS_2 ALD, and then annealed at 600 ºC in H_2S. Figure 17 shows TEM images of ~3 layers of MoS_2 on alumina coated MWCNTs. There was roughly 8 nm of alumina deposited on the corresponding MWCNTs prior to MoS_2 ALD. The nanotube walls are indicated by the green line spanning the MWCNT diameter and the blue bar indicates the alumina coating on one side of the MWCNT. The ALD

MoS_2 on the alumina is indicated by the red arrow. The spacing measured between the nanotube layers is ~0.37 nm, which can be expected, as shown from other studies[63, 64]. The MoS_2 region can be observed by the strong diffraction between the MoS_2 layers. The TEM image shows some amorphous material on the outmost surface of the MoS_2 in some regions along the perimeter of the tube, which is attributed to adventitious carbon that gathered on the sample prior to and during imaging.

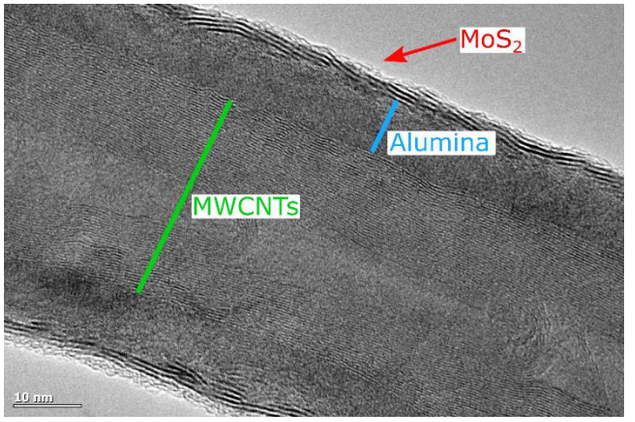

FIGURE 17. TEM image of multi-walled carbon nanotube with ~8 nm of alumina and ~3 layers of crystalline MoS_2 coating. To form a layered structure, the sample was annealed in H_2S at 600 ºC after 22 cycles of MoS_2 deposition at 200 ºC.

V. SUMMARY AND CONCLUSIONS

We have investigated the nucleation of ALD MoS_2 using H_2S and MoF_6 on three metal oxide surfaces and at a range of growth temperatures. Hydroxyl groups were shown to play a role in the chemisorption of MoF_6, where the QCM mass increase after the initial MoF_6 pulse was dependent on deposition temperature. This behavior indicates there was more chemisorption of MoF_6 at lower temperatures due to the higher concentration of OH groups. FTIR measurements show the initial formation of $MoOF_4$ species after the first MoF_6 exposure. Single

MoF_6 dose XPS studies on alumina, hafnia, and magnesia surfaces show MoO_3 and metal-F bonding is favorable. Additionally, density functional theory modeling supports formation of metal-F bonding and lack of byproduct production upon MoF_6 relaxation above a hydroxylated alumina surface. The second half-cycle of the MoS_2 ALD chemistry was probed by studying the byproducts after the H_2S dose. Residual gas analysis showed the formation of H_2O and HF byproducts after the first H_2S exposure. During subsequent MoS_2 ALD cycles, FTIR absorbance spectra showed the formation MoO_x in the range of 995-820 cm^{-1}. The MoO_x growth diminishes in later cycles indicating that Mo-O bond formation is limited by the availability of surface oxygen. Broadband FTIR absorbance spectra additionally gave insight into Mo-S bond formation by the increase in free carriers following H_2S exposures. XPS spectra acquired after 50 cycles of MoS_2 showed higher concentrations of S with increasing deposition temperature. High resolution XPS spectra of the Mo 3d and S 2p regions revealed a combination of MoO_2, MoO_3, and MoS_2. A relative decrease in MoO_x concentration was shown at the elevated temperatures. Growth temperature played a crucial role in morphology of films when increasing from 150 to 250 °C. At 250 °C, films showed a much higher degree of crystallinity, and exhibited vertical flakes as characterized by TEM, AFM, and Raman spectroscopy. Lastly, thin MoS_2 films were formed through two different processing conditions. These results highlight the relationship between growth temperature and film thickness. After annealing, these films were crystalline and were approximately three layers thick.

Progress towards integration of 2D materials in electronic applications requires the nucleation and growth to be well understood. Film nucleation, grain size, morphology, and substrate interface can all effect the final properties of deposited thin films. This work helps address these poorly understood stages of MoS_2 ALD. Here, we studied the early bonding and

heteronucleation between the ALD precursors and metal oxide substrates. This understanding can help identify what interfacial films may be forming during the growth process and can give insight into potential performance of our films. Additionally, this work helps identify the significance and effect that growth temperatures can have on nucleation and crystallization. These insights provide pathways toward greater control over thermal ALD of MoS_2 thin films for potential applications. Future work will integrate our thermal MoS_2 films in devices for electrical characterization and study crystalline growth at temperatures of 250 °C and above.

ACKNOWLEDGMENTS

This work was supported in part by NSF CAREER grant no. 1751268 and the NSF Center for Atomically Thin Multifunctional Coatings (ATOMIC) IUCRC (grant no. 2113873). FIB, TEM experiments were performed at the Microscopy and Characterization Suite (MaCS), Center for Advanced Energy Studies (CAES) under the support of MaCS Seed Grant MSG 22-001. A portion of this work was supported as part of the Center for Electrochemical Energy Science, an Energy Frontier Research Center funded by the U.S. Department of Energy (DOE), Office of Science, Office of Basic Energy Sciences. S.L. acknowledges support from the U.S. Department of Energy, Office of Science, Office of Workforce Development for Teachers and Scientists, Office of Science Graduate Student Research (SCGSR) program. The SCGSR program is administered by the Oak Ridge Institute for Science and Education for the DOE under Contract No. DE-SC0014664. Use of the Center for Nanoscale Materials, an Office of Science user facility, was supported by the U.S. Department of Energy, Office of Science, Office of Basic Energy Sciences, under Contract No. DE-AC02-06CH11357. This research made use of the resources of the High-Performance Computing Center at Idaho National Laboratory, which is supported by the Office of Nuclear Energy of the U.S. Department of Energy and the Nuclear

Science User Facilities under Contract No. DE-AC07-05ID14517. We would also like to acknowledge high-performance computing support of the R2 compute cluster (DOI: 10.18122/B2S41H) provided by Boise State University's Research Computing Department. We would like to thank Dr. Karthik Chinnathambi in the Boise State Center for Materials characterization for assistance with TEM imaging. Atomic force microscopy was performed in the Boise State University Surface Science Laboratory.

AUTHOR DECLARATIONS

Conflict of Interest

The authors have no conflicts to disclose.

DATA AVAILABILITY

The data that support the described findings are available within the primary article and the supplementary material.

REFERENCES

1. U. Krishnan, M. Kaur, K. Singh, M. Kumar and A. Kumar, Superlattice. Microst. **128**, 274-297 (2019).

2. S. Maulik, S. Basu, K. Kanakamedala and T. Daniels-Race, J. Electron. Mater. **48**, 3451-3458 (2019).

3. Y. Kim, W. J. Woo, D. Kim, S. Lee, S. m. Chung, J. Park and H. Kim, Adv. Mater. **33**, 2005907 (2021).

4. Y. L. Huang, Y. Chen, W. Zhang, S. Y. Quek, C.-H. Chen, L.-J. Li, W.-T. Hsu, W.-H. Chang, Y. J. Zheng, W. Chen and A. T. S. Wee, Nat. Commun. **6**, 6298 (2015).

5. B. Radisavljevic, A. Radenovic, J. Brivio, V. Giacometti and A. Kis, Nat. Nanotechnol. **6**, 147-150 (2011).

6. X. Zhang, N. Biekert, S. Choi, C. H. Naylor, C. De-Eknamkul, W. Huang, X. Zhang, X. Zheng, D. Wang, A. T. C. Johnson and E. Cubukcu, Nano Lett. **18**, 957-963 (2018).

7. T. Tajima, S. Okabe and Y. Takaguchi, B. Chem. Soc. Jpn. **93**, 745-750 (2020).

8. S. Yang, J. Cha, J. C. Kim, D. Lee, W. Huh, Y. Kim, S. W. Lee, H.-G. Park, H. Y. Jeong, S. Hong, G.-H. Lee and C.-H. Lee, Nano Lett. **20**, 2443–2451 (2020).

9. A. Jäger-Waldau, M. C. Lux-Steiner and E. Bucher, Solid State Phenom. **37-38**, 479-484 (1994).

10. Z. Huang, T. Zhang, J. Liu, L. Zhang, Y. Jin, J. Wang, K. Jiang, S. Fan and Q. Li, ACS Appl. Electron. Mater. **1**, 1314-1321 (2019).

11. Y. Xue, Q. Zhang, W. Wang, H. Cao, Q. Yang and L. Fu, Adv. Energy Mater. **7**, 1602684 (2017).

12. T. Tang, T. Zhang, L. Zhao, B. Zhang, W. Li, J. Xu, L. Zhang, H. Qiu and Y. Hou, Mater. Chem. Front. **4**, 1483-1491 (2020).

13. Q. Yun, Q. Lu, X. Zhang, C. Tan and H. Zhang, Angew. Chem.-Int. Edit. **57**, 626-646 (2018).

14. P. Yang, X. Zou, Z. Zhang, M. Hong, J. Shi, S. Chen, J. Shu, L. Zhao, S. Jiang and X. Zhou, Nat. Commun. **9**, 1-10 (2018).

15. J. Jeon, S. K. Jang, S. M. Jeon, G. Yoo, Y. H. Jang, J.-H. Park and S. Lee, Nanoscale **7**, 1688-1695 (2015).

16. A. Tarasov, P. M. Campbell, M. Y. Tsai, Z. R. Hesabi, J. Feirer, S. Graham, W. J. Ready and E. M. Vogel, Adv. Funct. Mater. **24**, 6389-6400 (2014).

17. H. Li, Q. Zhang, C. C. R. Yap, B. K. Tay, T. H. T. Edwin, A. Olivier and D. Baillargeat, Adv. Funct. Mater. **22**, 1385-1390 (2012).

18. R. L. Puurunen, J. Appl. Phys. **97**, 121301 (2005).

19. D. Zhou, H. Shu, C. Hu, L. Jiang, P. Liang and X. Chen, Cryst. Growth Des. **18**, 1012-1019 (2018).

20. H. Xue, G. Wu, B. Zhao, D. Wang, X. Wu and Z. Hu, ACS Appl. Electron. Mater. **2**, 1925-1933 (2020).

21. V. T. Nguyen, Y. C. Kim, Y. H. Ahn, S. Lee and J.-Y. Park, Carbon **168**, 580-587 (2020).

22. C. Ahn, Y. Park, S. Shin, J.-G. Ahn, I. Song, Y. An, J. Jung, C. S. Kim, J. H. Kim, J. Bang, D. Kim, J. Baik and H. Lim, ACS Appl. Mater. Inter. **13**, 6805-6812 (2021).

23. L. Huang, Q. H. Thi, F. Zheng, X. Chen, Y. W. Chu, C.-S. Lee, J. Zhao and T. H. Ly, J. Am. Chem. Soc. **142**, 13130-13135 (2020).

24. J. W. Elam, M. D. Groner and S. M. George, Rev. Sci. Instrum. **73**, 2981-2987 (2002).

25. R. A. Wind and S. M. George, J. Phys. Chem. A **114**, 1281-1289 (2010).

26. C. Berthomieu and R. Hienerwadel, Photosynth. Res. **101**, 157-170 (2009).

27. J. H. Lee, J. H. Eun, S. G. Kim, S. Y. Park, M. J. Lee and H. J. Kim, J. Mater. Res. **18**, 2895-2903 (2003).

28. S. H. Moon, T. W. Heo, S. Y. Park, J. H. Kim and H. J. Kim, J. Electrochem. Soc. **154**, J408 (2007).

29. S. Letourneau, M. J. Young, N. M. Bedford, Y. Ren, A. Yanguas-Gil, A. U. Mane, J. W. Elam and E. Graugnard, ACS Appl. Nano Mater. **1**, 4028-4037 (2018).

30. J. Ferguson, A. Weimer and S. George, Thin Solid Films **371**, 95-104 (2000).

31. J. W. Elam, J. A. Libera and J. N. Hryn, Ecs Transactions **41**, 147 (2011).

32. A. Yanguas-Gil, J. A. Libera and J. W. Elam, ECS Transactions **50**, 43-51 (2013).

33. D. M. Hausmann, E. Kim, J. Becker and R. G. Gordon, Chem. Mater. **14**, 4350-4358 (2002).

34. B. Burton, D. Goldstein and S. George, J. Phys. Chem. C **113**, 1939-1946 (2009).

35. C. Nelson, J. Elam, M. Cameron, M. Tolbert and S. George, Surf. Sci. **416**, 341-353 (1998).

36. D. Seghete, G. Rayner Jr, A. Cavanagh, V. Anderson and S. George, Chem. Mater. **23**, 1668-1678 (2011).

37. M. Lawson, E. Graugnard and L. Li, Appl. Surf. Sci. **541**, 148461 (2021).

38. L. E. Alexander, I. R. Beattie, A. Bukovszky, P. J. Jones, C. J. Marsden and G. J. V. Schalkwyk, J. Chem. Soc. Dalton, 81-84 (1974).

39. S. Chempath, Y. Zhang and A. T. Bell, J. Phys. Chem. C **111**, 1291-1298 (2007).

40. C. E. Nanayakkara, A. Vega, G. Liu, C. L. Dezelah, R. K. Kanjolia and Y. J. Chabal, Chem. Mater. **28**, 8591-8597 (2016).

41. T. Hirata, Appl. Surf. Sci. **40**, 179-181 (1989).

42. Y. Lee, J. W. DuMont, A. S. Cavanagh and S. M. George, J. Phys. Chem. C **119**, 14185-14194 (2015).

43. J. W. Elam, A. U. Mane, J. A. Libera, J. N. Hryn, O. H. Siegmund, J. McPhate, M. J. Wetstein, A. Elagin, M. J. Minot and A. O'Mahony, ECS Transactions **58**, 249-261 (2013).

44. C. Chang and S. Chan, J. Catal. **72**, 139-148 (1981).

45. M. Morales-Luna, S. A. Tomás, M. A. Arvizu, M. Pérez-González and E. Campos-Gonzalez, J. Alloy Compd. **722**, 938-945 (2017).

46. V. Dřínek, M. Klementová, L. Palatinus, P. Dytrych, R. Fajgar, V. Jandová, M. Koštejn and J. Kupčík, J. Alloy Compd. **808**, 151470 (2019).

47. M. Shirazi and S. D. Elliott, Nanoscale **7**, 6311-6318 (2015).

48. W. R. Smith, J. Chem. Inf. Comp. Sci. **36**, 151-152 (1996).

49. S. I. Castañeda, I. Montero, J. M. Ripalda, N. Díaz, L. Galán and F. Rueda, J. Appl. Phys. **85**, 8415-8418 (1999).

50. A. U. Mane, S. Letourneau, D. J. Mandia, J. Liu, J. A. Libera, Y. Lei, Q. Peng, E. Graugnard and J. W. Elam, J. Vac. Sci. Technol. A **36** (2018).

51. R. L. Puurunen and W. Vandervorst, J. Appl. Phys. **96**, 7686-7695 (2004).

52. P. Kumar, M. Singh and G. Reddy, Mater. Res. Express **4**, 036405 (2017).

53. L. Benoist, D. Gonbeau, G. Pfister-Guillouzo, E. Schmidt, G. Meunier and A. Levasseur, Thin Solid Films **258**, 110-114 (1995).

54. D. Ganta, S. Sinha and R. T. Haasch, Surf. Sci. Spectra **21**, 19-27 (2014).

55. A. M. De Jong, H. J. Borg, L. J. Van Ijzendoorn, V. Soudant, V. H. J. De Beer, J. A. R. Van Veen and J. W. Niemantsverdriet, The Journal of Physical Chemistry **97**, 6477-6483 (1993).

56. W. M. Parkin, A. Balan, L. Liang, P. M. Das, M. Lamparski, C. H. Naylor, J. A. Rodríguez-Manzo, A. C. Johnson, V. Meunier and M. Drndic, ACS Nano **10**, 4134-4142 (2016).

57. Z. Kou, A. Hashemi, M. J. Puska, A. V. Krasheninnikov and H.-P. Komsa, npj Comput. Mater. **6**, 1-7 (2020).

58. S. Balasubramanyam, M. A. Bloodgood, M. van Ommeren, T. Faraz, V. Vandalon, W. M. Kessels, M. A. Verheijen and A. A. Bol, ACS Appl. Mater. Inter. **12**, 3873-3885 (2019).

59. A. Sharma, M. A. Verheijen, L. Wu, S. Karwal, V. Vandalon, H. C. Knoops, R. S. Sundaram, J. P. Hofmann, W. E. Kessels and A. A. Bol, Nanoscale **10**, 8615-8627 (2018).

60. R. Ganatra and Q. Zhang, ACS Nano **8**, 4074-4099 (2014).

61. C. Lee, H. Yan, L. E. Brus, T. F. Heinz, J. Hone and S. Ryu, ACS Nano **4**, 2695-2700 (2010).

62. E. Mercado, A. Goodyear, J. Moffat, M. Cooke and R. S. Sundaram, J. Phys. D Appl. Phys. **50**, 184005 (2017).

63. C. H. Kiang, M. Endo, P. M. Ajayan, G. Dresselhaus and M. S. Dresselhaus, Phys. Rev. Lett. **81**, 1869-1872 (1998).

64. M. Bretz, B. G. Demczyk and L. Zhang, J. Cryst. Growth **141**, 304-309 (1994).

TABLE 5. Reaction equations representative of the MoF_6 half-reaction on Al2O3.

$Al_2O_3 + MoF_6(g) \rightarrow 2AlF_3 + MoO_3;\ \Delta G = -442\ \frac{kJ}{mol\ Mo}$	Eq. 2
$Al_2O_3 + 3MoF_6(g) \rightarrow 2AlF_3 + 3MoOF_4;\ \Delta G = -186\ \frac{kJ}{mol\ Mo}$	Eq. 3
$Al(OH)_3 + MoF_6(g) \rightarrow AlF_3 + 3MoO_3 + 3HF(g);\ \Delta G = -357\ \frac{kJ}{mol\ Mo}$	Eq. 4
$Al(OH)_3 + 3MoF_6(g) \rightarrow AlF_3 + 3MoOF_4 + 3HF(g);\ \Delta G = -158\ \frac{kJ}{mol\ Mo}$	Eq. 5
$2Al(OH)_3 \rightarrow Al_2O_3 + H_2O(g);\ \Delta G = -35\ \frac{kJ}{mol\ Al}$	Eq. 6

TABLE 6. Reaction representative of the H_2S half reaction on Al_2O_3.

$MoO_3 + 3H_2S(g) \rightarrow MoS_2 + 3H_2O(g) + S;\ \Delta G = -180\ \frac{kJ}{mol}$	Eq. 7
$MoOF_4 + 3H_2S(g) \rightarrow MoS_2 + 4HF(g) + H_2O(g) + S;\ \Delta G = -318\ \frac{kJ}{mol}$	Eq. 8

TABLE 7. Atomic percentages from XPS survey scans after 50 cycles of as-deposited MoS_2 ALD on alumina.

Sample	C 1s	O 1s	F 1s	Al 2p	S 2p	Mo 3d
150 ºC	6.57	26.25	9.85	39.68	8.75	8.9
200 ºC	6.97	21.4	9.79	37.23	12.85	11.76
250 ºC	0.31	5.93	6.71	1.65	51.78	33.63

TABLE 8. Atomic percentages from XPS high-resolution scans of as-deposited 50 cycles MoS_2 ALD on alumina.

	150 °C		200 °C		250 °C	
Atomic %	Mo 3d	S 2s	Mo 3d	S 2s	Mo 3d	S 2s
MoS_2	5.61	44.9	19.56	66.24	31.12	74.92
MoO_x	83.27		63.45		51.4	
MoO_xS_y	8.92		7.8		1.4	
S_x		55.11		33.77		25.08

FIGURE 4. *In situ* QCM measurements of mass versus time for the first few cycles of MoS_2 ALD on alumina. Mass change for initial MoF_6 pulse can be seen for deposition temperatures of 150, 200, and 250 ºC. MoF_6 and H_2S pulses are indicated schematically. Temperature dependent mass gains can be observed with 150 ºC deposition temperature having the most initial mass gain after MoF_6.

FIGURE 2. FTIR difference spectra for the last alumina cycle at 200 ºC and first two cycles of MoS_2 deposited at 150, 200, and 250 ºC. Plots (a-c) show the full spectra, where the OH stretches of the last water pulse (in red) can be seen above 3500 cm^{-1}. Plots (d-f) show expanded views of lower frequency portion of the spectra from 1500 to 550 cm^{-1} to highlight changes in the Al-O bulk modes and appearance of a $MoOF_4$ mode near 1039 cm^{-1}. Spectra are offset vertically for clarity.

FIGURE 3. *In situ* FTIR absorption measurements at (a) 150, (b) 200, and (c) 250 ºC. In each, the first two spectra, in red and black, are the final TMA and H_2O ALD half-cycles. Subsequent cycle precursor and number are labeled to the right of the axes. As indicated by the labels and dashed lines, peaks appear at ~1039 cm^{-1} following exposure to MoF_6, which we assign to the formation of $MoOF_4$ following Ref. 39 and 40. Spectra are offset for clarity.

FIGURE 4. High resolution XPS scans of F 1s on (a) alumina, (b) hafnia, (c) magnesia and Mo 3d peaks on (d) alumina, (e) hafnia, (f) magnesia after a single MoF_6 dose on metal oxide surfaces

at 200 ºC. Peak fitting reveals metal fluoride bonding is favorable on each metal oxide substrate as well as MoO_3 bonding.

FIGURE 5. Atomic models resulting from density functional theory (DFT) simulations of the relaxed system (a) and charge density difference (b) of an alumina surface with two MoF_6 precursors. The MoF_6 precursors are numbered 1 and 2 to help distinguish how each reacts with the surface. Cyan and yellow isosurfaces indicate a gain or loss of electrons, respectively. Precursor 1 shows MoFx-O formation. Fluorine atoms from precursor 2 are shown bonding to Al atoms indicating favorable Al-F bonding.

FIGURE 6. DFT atomic models of the relaxed system (a) and charge density difference (b) of an alumina surface with three MoF_6 precursors. The MoF_6 precursors are numbered 1, 2, and 3 to help distinguish how each reacts with the surface. Cyan and yellow isosurfaces indicate a gain or loss of electrons, respectively. The addition of a third MoF_6 promotes both AlF_3 and $MoOF_4$ bonds.

FIGURE 7. Residual gas analysis intensities for H_2O (m/e = 18), HF (m/e = 20), and F_2 (m/e = 38) during the first cycle of MoS_2 ALD on alumina at 200 ºC. Gaseous H_2O was the primary byproducts observed after during the first MoF_6 exposure. HF and possibly H_2O can be observed as byproducts from the H_2S reaction. Vertical black dashed line indicates beginning of MoF_6 pulses and the grey vertical dashed line indicates beginning of H_2S dosing. Six consecutive doses of each precursor were conducted during experiment.

FIGURE 8. Mass change per cycle for MoS_2 deposition at 150, 200, and 250 ºC on ALD alumina. Islanding formation and coalescence behavior is observed for each growth temperature.

FIGURE 9. *In situ* FTIR difference spectra of alumina after the first few MoS_2 cycles at 200 ºC. Plot range limited to 550-1500 cm^{-1} for clarity of peak mode detection. Key modes are labeled. Black and red difference spectra is from the last ALD cycle of substrate oxide. Blue and green spectra denote MoF_6 and H_2S dosing, respectively. Spectra are offset for clarity.

FIGURE 10. *In situ* FTIR absorbance for 10 cycles of MoS_2 on alumina. The absorbance was determined by the y-intercept of a horizontal line fit to 1725 to 1675 cm^{-1} region of the FTIR spectra at each temperature. Each data point represents a single half cycle. For reference, baseline data are included for the final TMA and H_2O exposures for the alumina ALD.

FIGURE 11. High resolution XPS spectra of the (a) Mo 3d and (b) S 2p regions of 50 cycles of as-deposited MoS_2 on ~20 nm ALD alumina at 150, 200, and 250 ºC. A decrease in the MoO_x peaks can be seen as the deposition temperature increased. This decrease in MoO_x is coupled with the increase in the MoS_2 bonding.

FIGURE 15. Film thickness measurements as measured by spectroscopic ellipsometry after 50 cycles of MoS_2 ALD on (a) alumina and (b) hafnia substrates. As-deposited films (black dashes) show an increase in thickness with growth temperature. The thickness of films is reduced after annealing (red dashes) in H_2S environment at 600 °C.

FIGURE 16. Raman spectroscopy scans of as-deposited (dashed line) and annealed (solid line) films after 50 cycles of MoS_2 ALD. An increase in intensity and decrease in FWHM of E^1_{2g} mode can be identified.

FIGURE 14. Atomic force microscope height images of as-deposited MoS_2 films grown with 50 cycles of ALD at 250 °C on (a) alumina, (b) hafnia, and (c) magnesia coated Si substrates. Topography results indicate the formation of vertical flakes for each surface.

FIGURE 15. Transmission electron microscope cross section images of MoS_2 films (a) deposited at 200 °C, then annealed at 600 °C for 30 min in H_2S and (b) as-deposited films at 250 °C. Crystalline MoS_2 domains are parallel to growth substrate when deposition temperature is 200 °C, followed by annealing, while vertical flakes can be identified from as-deposited films grown at 250 °C.

FIGURE 16. Raman spectra of MoS_2 thin films on alumina after (a) 22 cycles at 200 ºC and (b) 50 cycles at 160 ºC. Both films were annealed at 600 ºC in H_2S. Peak separation of 23 cm^{-1} between $A_{1g} - E^1_{2g}$ corresponds to a three-layer MoS_2 film.

FIGURE 17. TEM image of multi-walled carbon nanotube with ~8 nm of alumina and ~3 layers of crystalline MoS_2 coating. To form a layered structure, the sample was annealed in H_2S at 600 ºC after 22 cycles of MoS_2 deposition at 200 ºC.

Journal of Vacuum Science & Technology A

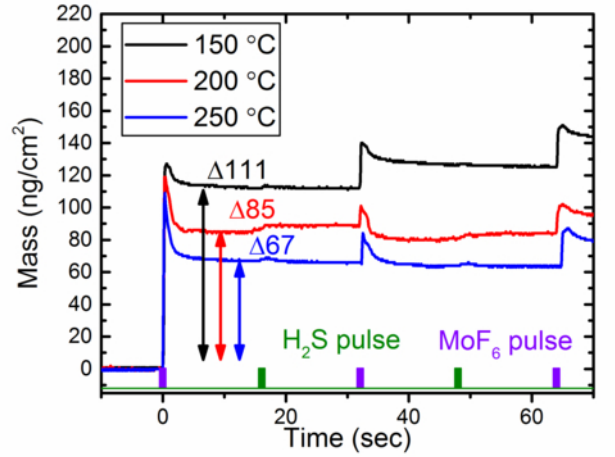

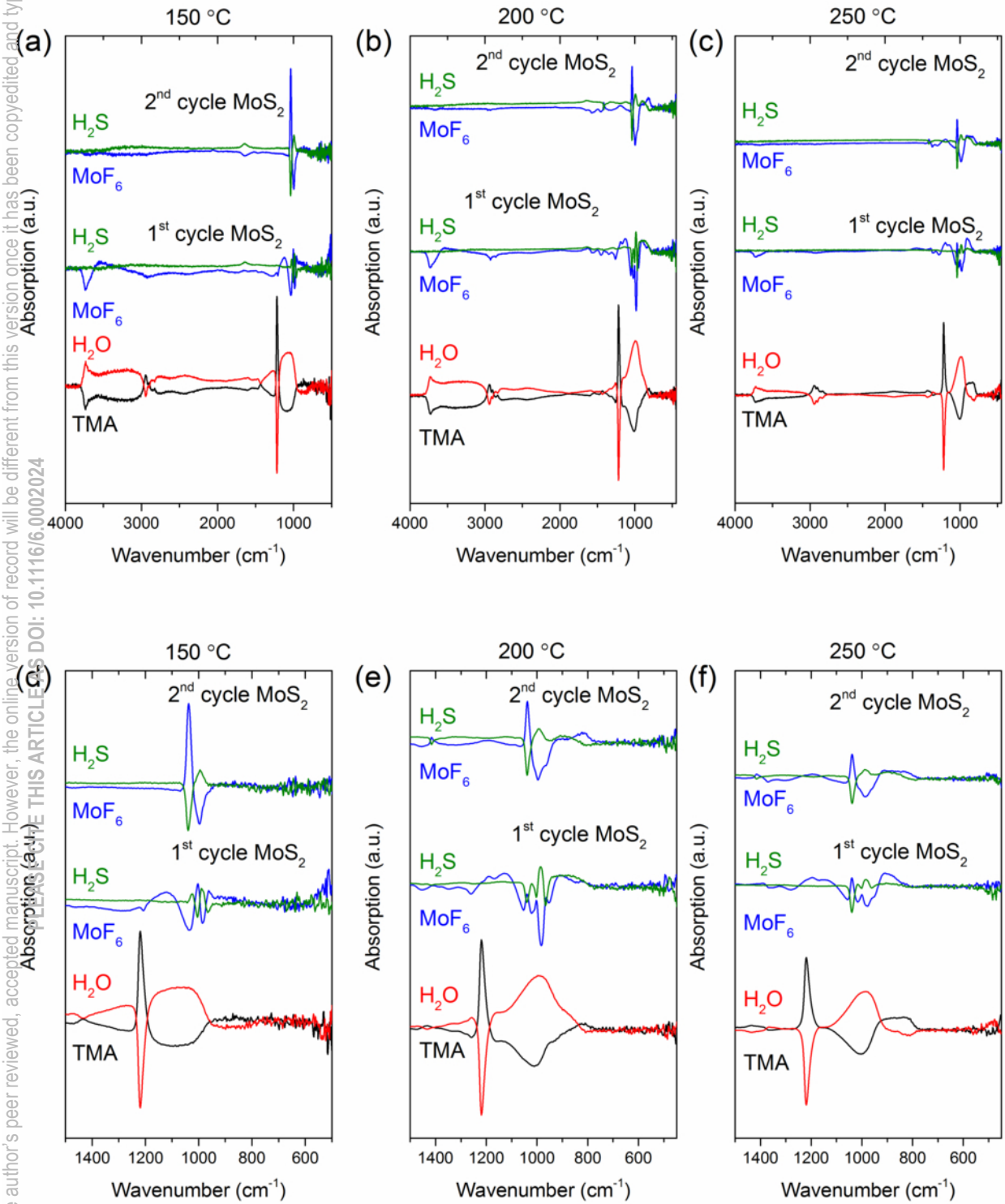

Journal of Vacuum Science & Technology A

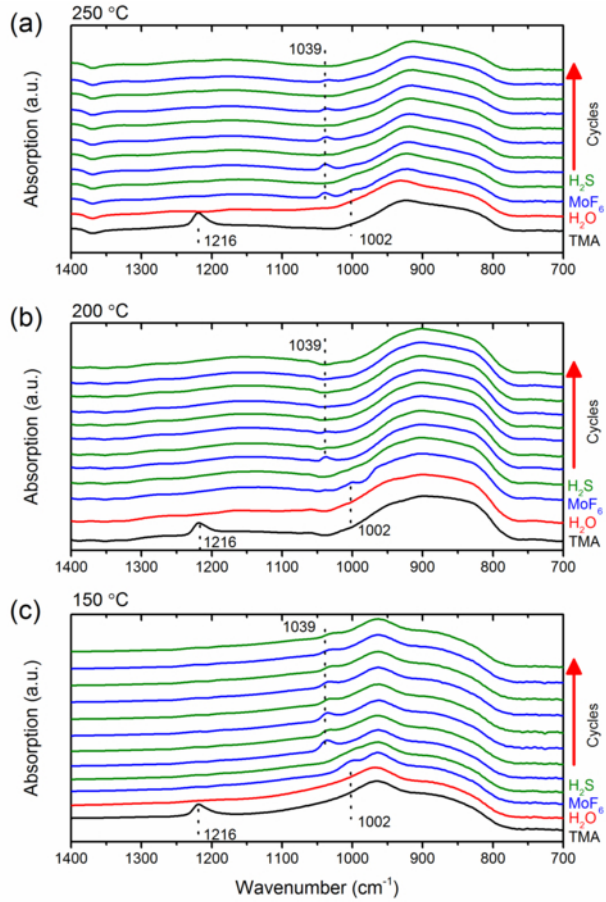

Journal of Vacuum Science & Technology A

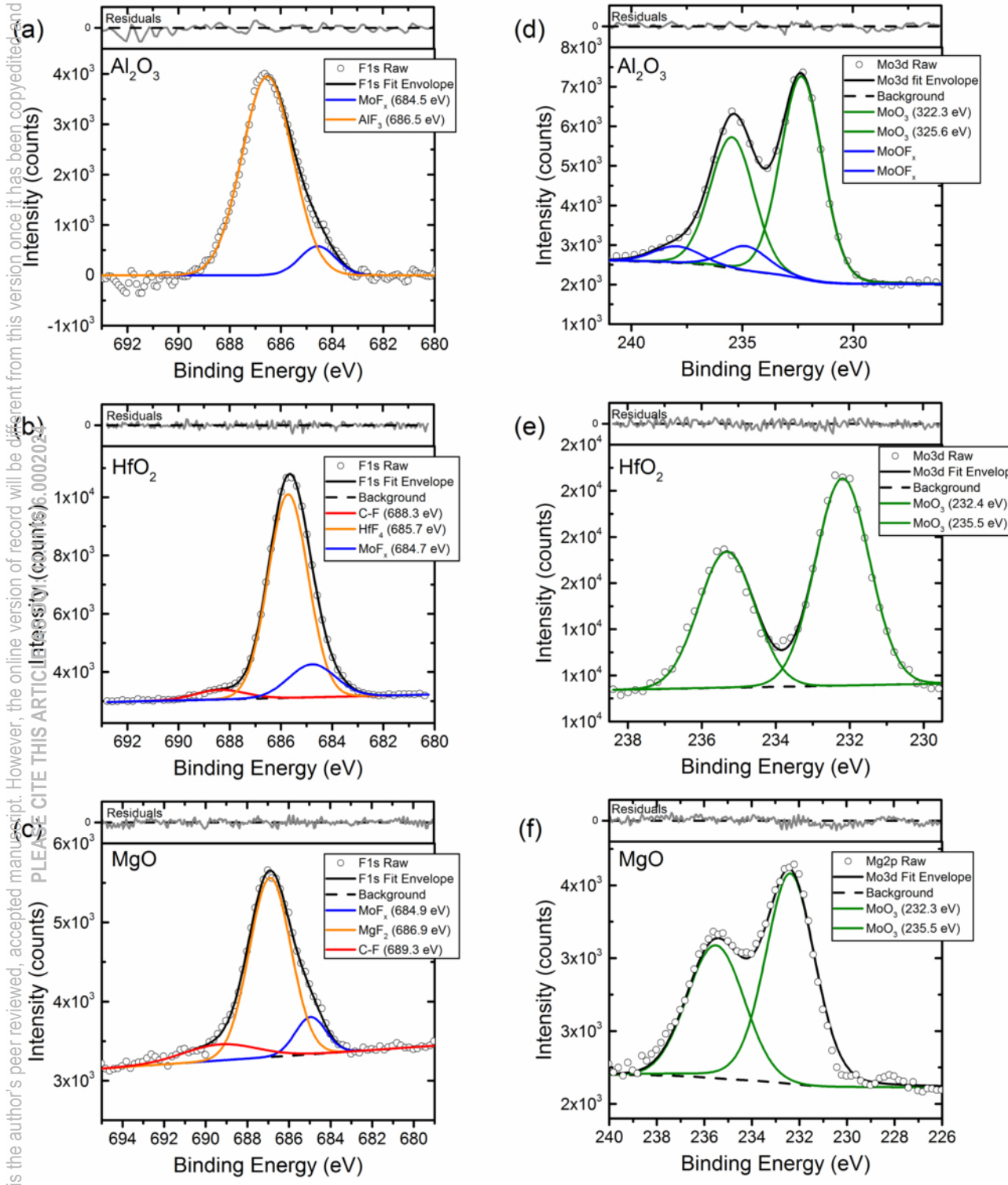

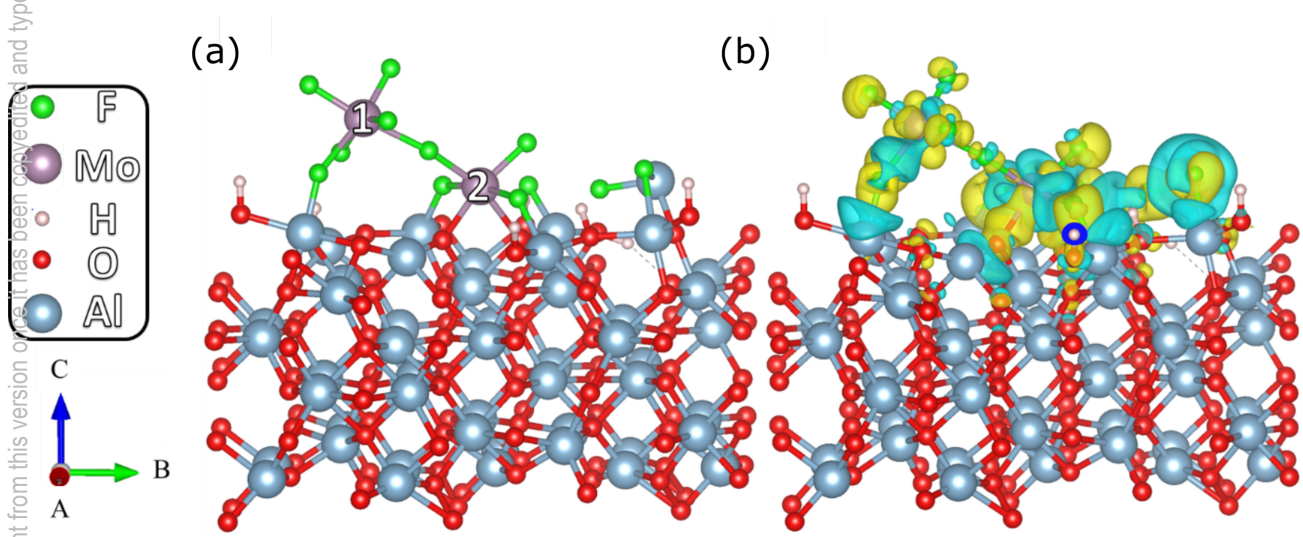

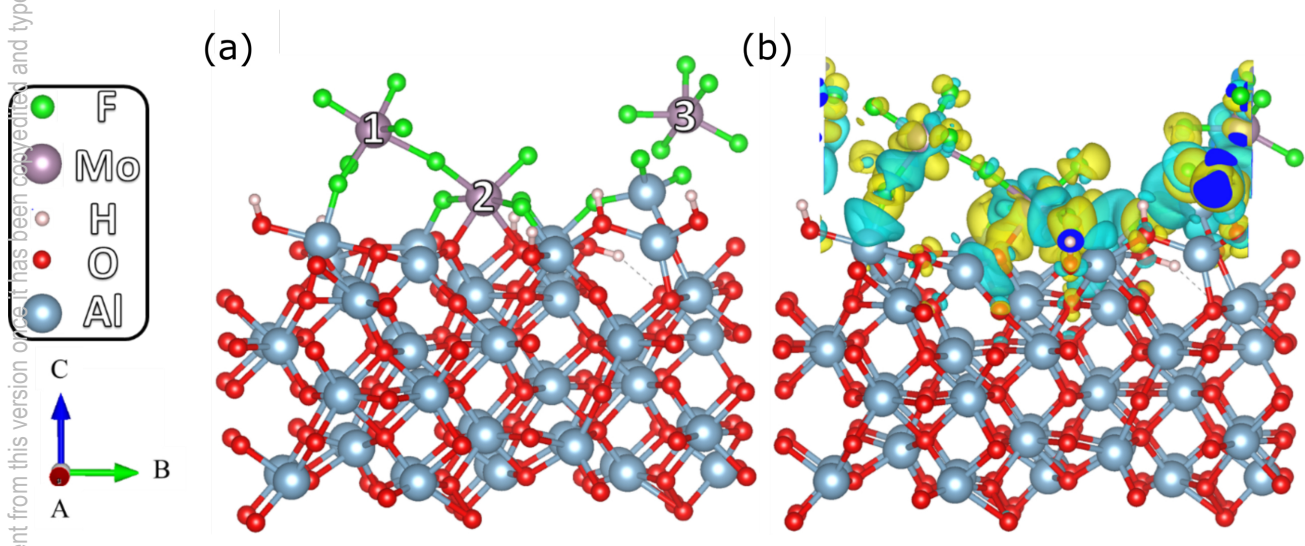

Journal of Vacuum Science & Technology A

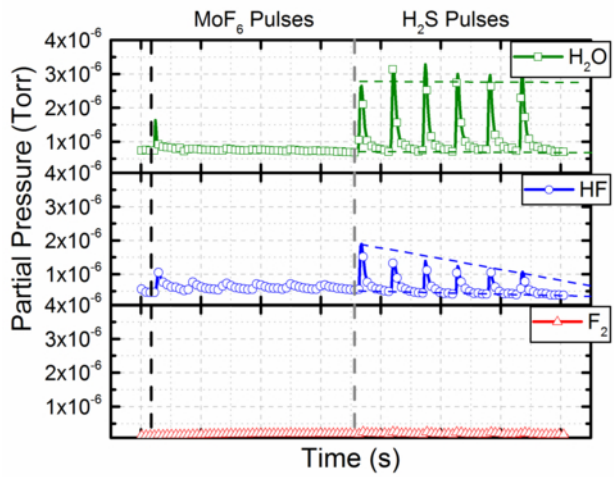

Journal of Vacuum Science & Technology A

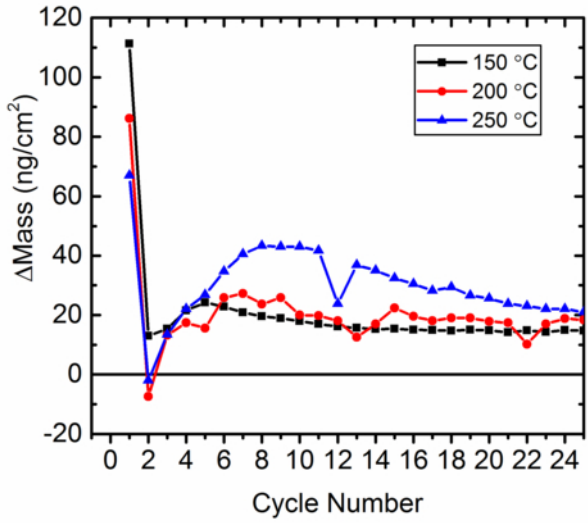

Journal of Vacuum Science & Technology A

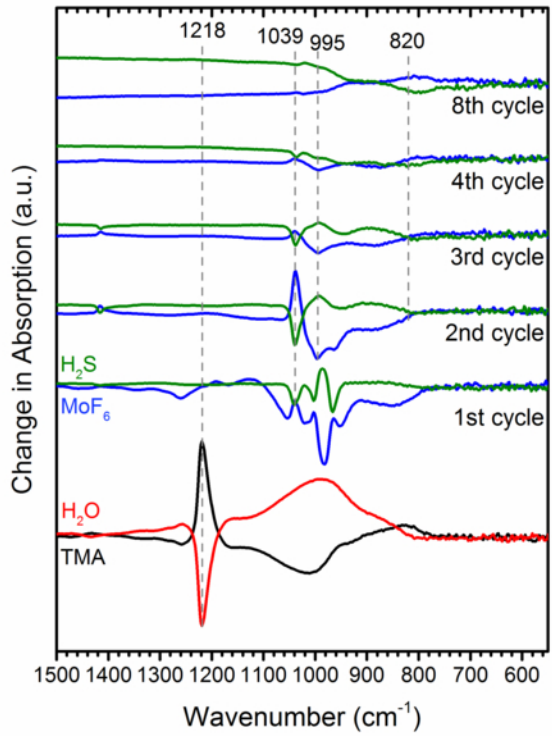

Journal of Vacuum Science & Technology A

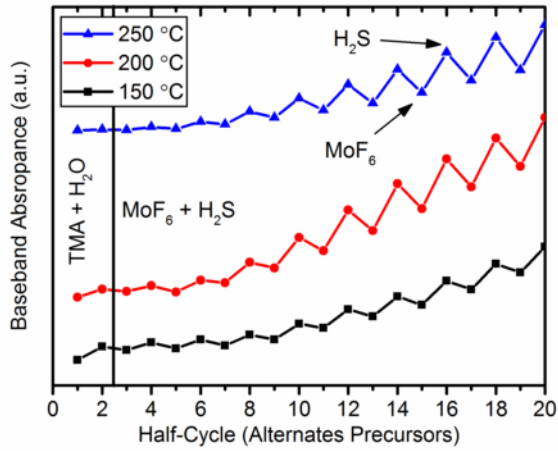

Journal of Vacuum Science & Technology A

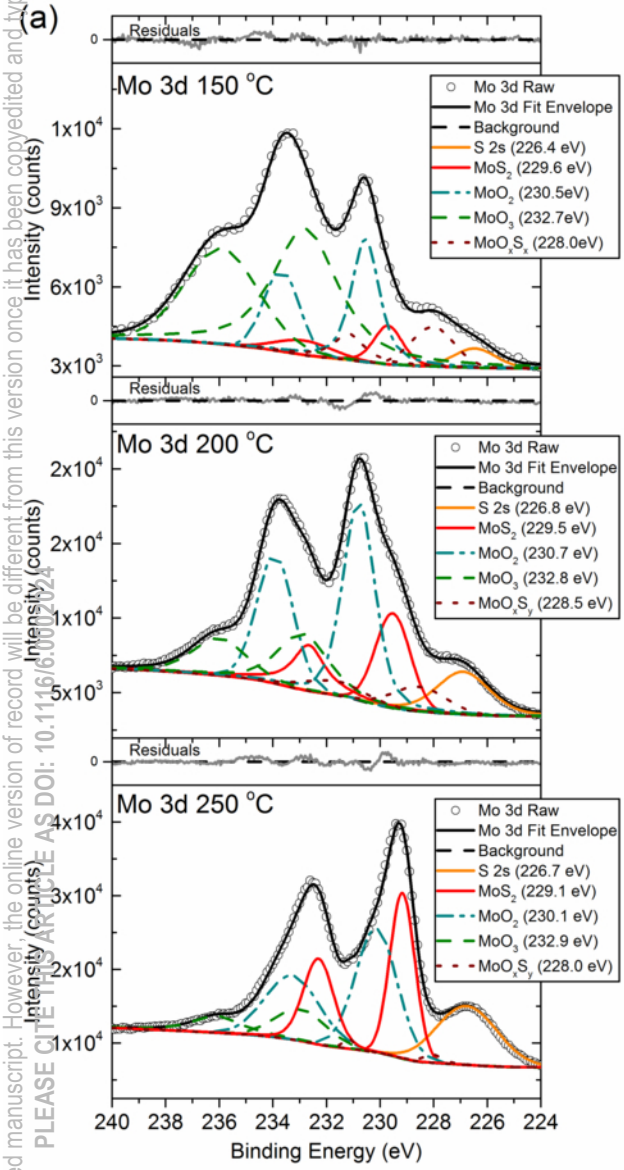

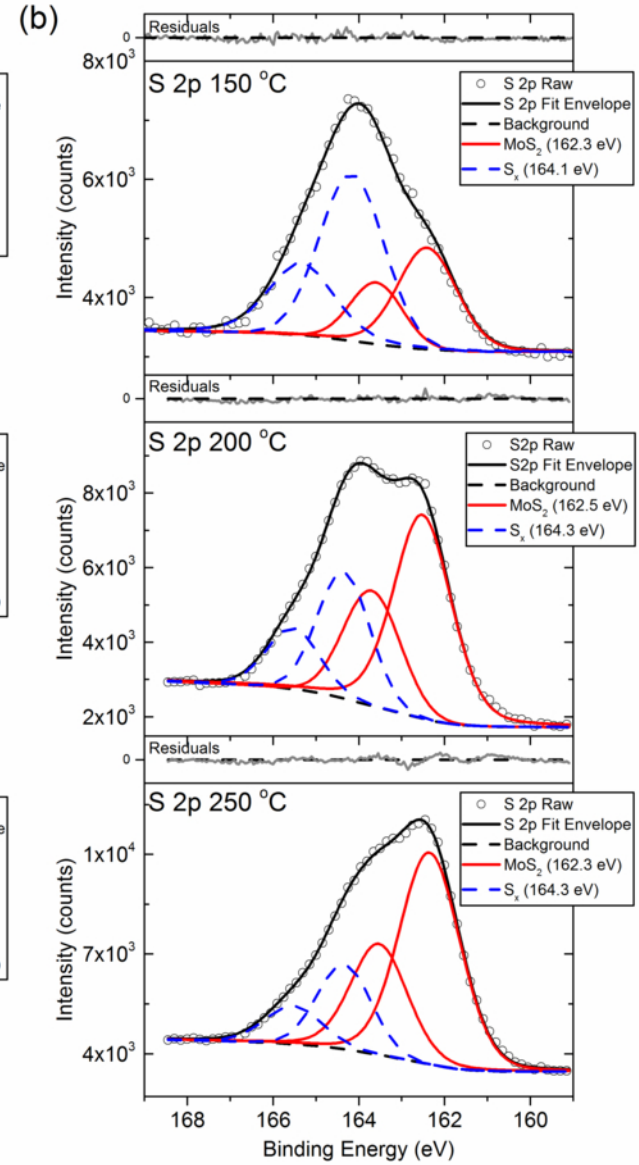

Journal of Vacuum Science & Technology A

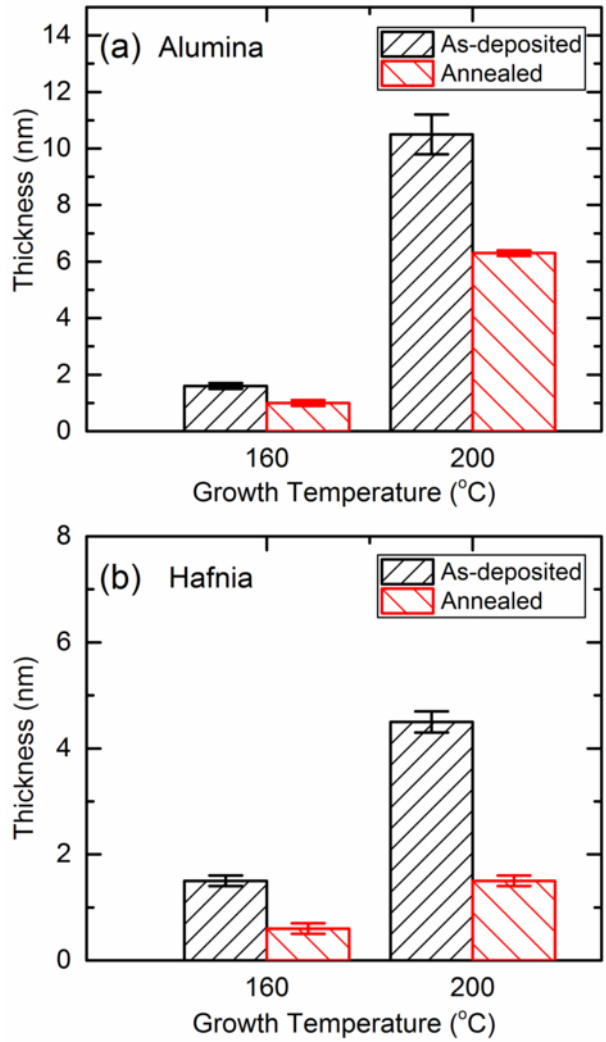

Journal of Vacuum Science & Technology A

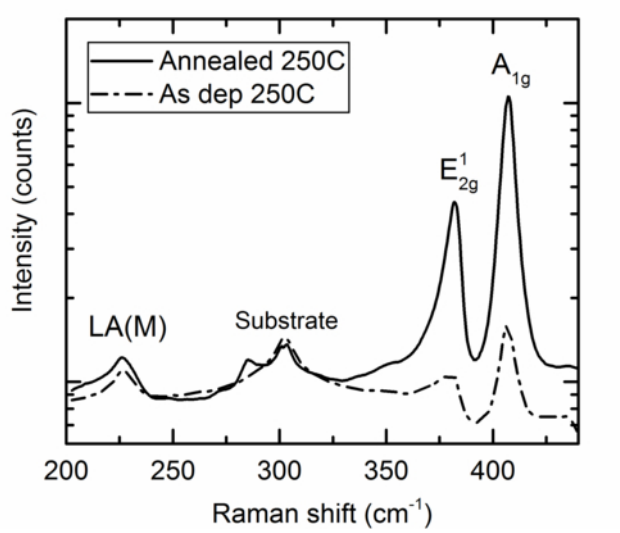

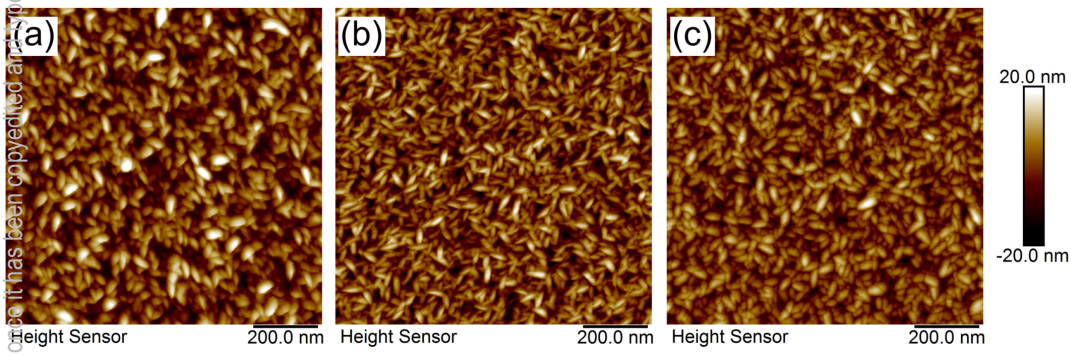

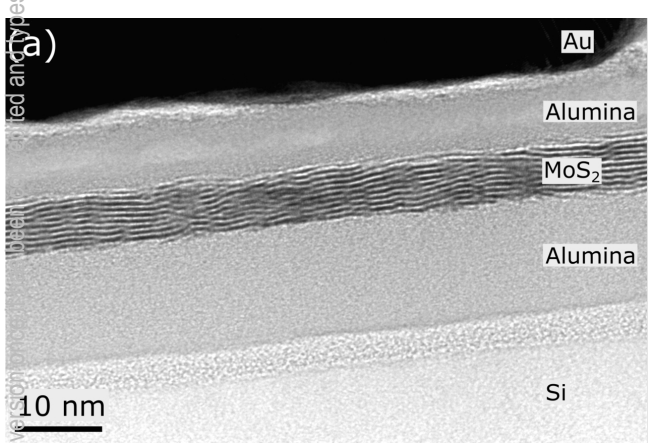

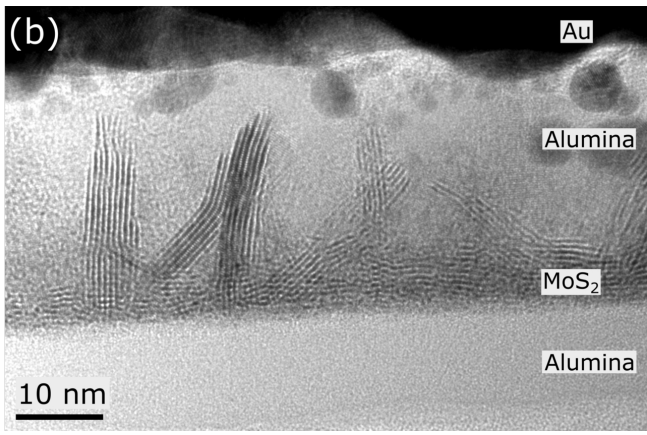

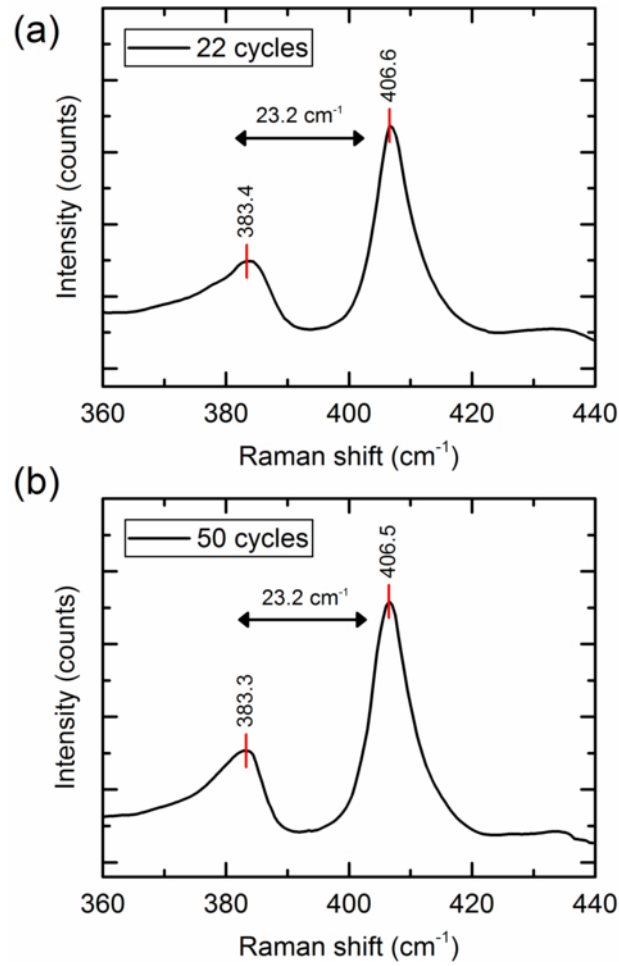

Journal of Vacuum Science & Technology A